University of Stavanger

AUTHOR: MOHSEN MOHAMMADI
SUPERVISOR: VIDAR FOLKE HANSEN

Strength enhancement of aluminium alloy 6082 for El car chassis through cold work and precipitation hardening

Bachelor thesis (Spring, 2024)
Engineering Structures and Materials / Mechanical Engineering
Faculty of Science and Technology
Department of Mechanical and Structural Engineering and Materials Science

Abstract

This thesis investigates the effect of cold rolling and precipitation hardening on the strength of aluminium alloy 6082. The material underwent several processes, including a solution heat treatment at 540 °C for 1 hour, three degrees of deformation, 0 %, 30 %, and 60 % after solution heat treatment, and artificial ageing at 180 °C for 8 hours after cold rolling. The effect of natural ageing was also briefly examined.

The results of mechanical tests such as the tensile and Vickers hardness tests revealed that cold rolling and precipitation hardening significantly increased the material's strength and affected mechanical properties such as hardness, tensile strength, yield strength, ductility, and toughness. Additionally, a clear effect of cold work on precipitation hardening was observed such that the impact of precipitation hardening on mechanical properties decreased as the degree of deformation increased.

The material's microstructure was analysed using an Optical and Scanning Electron Microscope. The results revealed noticeable changes in grain structure and size induced by cold rolling. The material's microstructure also showed signs of texture with a preferred grain orientation as the degree of deformation increased to 60 per cent.

Acknowledgement

I would like to express special thanks and appreciation to Ola Jensrud at Sintef for providing me with the material needed to perform this research.

I also want to thank my university supervisor, Professor Vidar Folke Hansen, who supported me with advice and careful supervision throughout this research.

I would also like to thank engineers Johan Andreas Thorkaas, Espen Undheim, and Mats Ingdal for helping me with laboratory and microscopic investigations. Without their help, conducting and concluding this research would have been impossible.

Finally, I would like to thank my classmates Torbjørn Nærland Wiig and Andreas Gingstad Pedersen, who helped me several times with the practical part of this research.

Contents

List of Figures

List of Tables

Abbreviations and Symbols

Symbol	Description
σ_y	Material's yield stress
σ_0	Constant for a particular material in Hall-Petch equation
k_y	Constant for a particular material in Hall-Petch equation
d	Average grain diameter in Hall-Petch equation
σ_{y0}	The initial yield strength
σ_{yi}	Yield strength after releasing the load, and then upon reloading
σ	Engineering stress
F	Applied load perpendicular to the specimen
A_0	Original cross-sectional area
A_f	Cross-sectional area at the fracture point
ϵ	Engineering strain
l_i	Instantaneous length
l_0	Original length
l_f	Fracture length
E	Modulus of elasticity (Young's modulus)
d	Arithmetic mean of the two diagonals in mm
HV	Hardness Vickers

θ	Angle of incidence of the X-rays or waves onto the crystal lattice.
n	An integer representing the order of the diffraction peak.
λ	Wavelength of the incident waves.
SEM	Scanning Electron Microscope
SE	Secondary Electrons
BSE	Backscattered Electrons
EDS	Energy Dispersive Spectroscopy
$EBSD$	Electron Backscatter Diffraction
TEM	Transmission Electron Microscope
PCR	Perpendicular to cold rolling
ACR	Along cold rolling
STD	Standard deviation

1 Introduction

Aluminium and its alloys are among the materials that are widely used in various industries such as aerospace, automotive and structural engineering. Recently, aluminium has been in high demand for electric cars. Features such as low density, corrosion resistance, and good thermal conductivity cause vehicle manufacturers to select aluminium as the first option in electric car parts. For instance, the low density of aluminium makes cars lightweight and, as a result, saves energy and increases the driving range. The thermal conductivity of aluminium contributes to heat dissipation and maintains an optimal temperature for the battery. However, the low strength of aluminium compared to other metals limits its utilization in high-stress applications such as the chassis of cars.

This thesis explores methods to enhance the strength of aluminium profiles for electric car chassis by cold work and precipitation hardening. The primary objective is to evaluate the effect of the combination of cold work, natural ageing and artificial ageing on the strength of aluminium profiles. The second objective is to investigate the effect of cold work on the precipitation hardening process.

The aluminium sample is a type of 6xxx series, namely

6082, provided by Santifet. The sample experienced a heat treatment solution for 60 minutes at 540 °C, cold rolling down to 0, 30 and 60 per cent reduction and a precipitation heat treatment at 180 °C for 8 hours. Further, the Vickers hardness test was performed to investigate the effect of natural and artificial ageing on the hardness of the material. A tensile test was also conducted to test the material's strength in the cold rolling direction and the vertical direction perpendicular to it. Both optical and Scanning electron microscopes were utilized to investigate the microstructure.

The thesis begins with a theory section, followed by an experimental section. It then continues with a result section illustrating all results, tables and measurements. The results will be discussed, and the thesis will end with a conclusion.

2 Theory

2.1 Metal alloys

Solid materials are divided into three main categories: Metals, Ceramics and Polymers[1]. Although metals exist both in pure and alloy form, alloys are used more in the industry due to the variety of their mechanical properties. Metal alloys, by composition, are often grouped into two classes, ferrous and nonferrous. Ferrous alloys, containing iron as the primary constituent, include steels and cast irons. Nonferrous alloys, on the other hand, are not iron-based[2].

In addition, alloys can also be classified based on some specific characteristics that a group of alloys represent. For instance, alloys can be classified based on the following groups[2]:

Cast alloys are those that are so brittle, and for this reason, it is not possible to form them with appreciable deformation.

Wrought alloys are those that demonstrate high deformability.

Heat-treatable alloys are those whose mechanical strength can be improved by precipitation hardening.

2.2 Aluminum alloys

Aluminium and its alloys have an FCC crystal structure with a low melting temperature of 660°C. They demonstrate low density, resistance to corrosion, and high conductivity, which make them highly desired in engineering applications. However, aluminium's mechanical strength is low compared to that of other metals like steel or titanium. Cold work and alloying are the solutions to enhance the strength of the aluminium. Cold work is not recommended for aluminium cast alloys because of their brittleness. Regarding alloying, elements mainly used to enhance the strength of aluminium include copper, magnesium, silicon, manganese, and zinc.
Further, a precipitation hardening process can harden heat-treatable alloys, while non-heat-treatable alloys will achieve high strength by a solid solution mechanism [3]. These mechanisms will be discussed in the following sections.

2.2.1 Alloy 6082

6082 is an aluminium alloy of 6xxx series. Alloys in this series typically contain magnesium (Mg) and silicon (Si) as primary alloying elements, which are required to form the magnesium silicide (Mg_2Si) phase. The presence of

this phase is essential since it makes the 6xxx series heat-treatable. 6xxx series has high corrosion resistance with a medium strength property. They also have good formability, machinability and weldability [4]. 6082 is not an exception in this series and has, in addition, the highest strength among other types of this series. This alloy is usually used in many applications, such as High-stress applications, Trusses, Bridges, Cranes, Transport applications, etc [5].

2.3 Heat treatments

Several heat treatments exist in material technology. This thesis will cover the most relevant ones to the topic of this thesis, including solution heat treatment and precipitation heat treatment.

2.3.1 Solution heat treatment (SHT)

Solution heat treatment is a heat-treating process that heats alloys to a specific temperature and holds them at that temperature for a time to create a single-phase solid solution. After this, the alloy is rapidly cooled or quenched to a much lower temperature (for most alloys, room temperature) to maintain the single-phase structure formed during the SHT process, which is critical to attaining high-quality mechanical properties such as

hardness and strength in further processes such as cold work and precipitation heat treatment[6]. The coolant and cooling rate can vary and depend on the alloy and the conditions of the experiment.

2.3.2 Preciptation heat treatment

Precipitation heat treatment is the second heat treatment in the precipitation hardening process after solution heat treatment. The process involves heating the supersaturated solid solution to an intermediate temperature below the melting point and holding it for a specific time (ageing time). The temperature is less than the SHT temperature, and the ageing time is longer than required for the SHT process. During ageing, small particles of a new phase will start to grow within the solid solution matrix. These particles are responsible for enhancing the strength of the material[1]. If the ageing process occurs at room temperature, it is called natural ageing. However, If the process occurs at a higher temperature than room temperature but below the melting point, it is called artificial ageing. Artificial ageing causes particles to grow faster than natural ageing [7].

[1]More details are discussed in section 2.5.4.

2.4 Some basic concepts in hardening mechanisms

This section will cover some basic concepts that can be useful in understanding hardening mechanisms better.

2.4.1 Crystalline defect

Crystalline defects are defined as imperfections in the regular geometrical arrangement of atoms in a crystalline solid. Defects can be created by deformation of the material, rapid cooling (quenching) from high temperatures, and high-energy radiation (X-ray) striking the crystalline solid. There are different types of defects, such as point defects, linear defects, surface defects, and volume defects [8].

2.4.2 Vacancy

Vacancy is a type of point defect created when an atom is missing in the crystal. All crystalline solids contain vacancies, and creating a material without them is impossible [9]. Figure 2.1 indicates a vacancy in a crystalline solid.

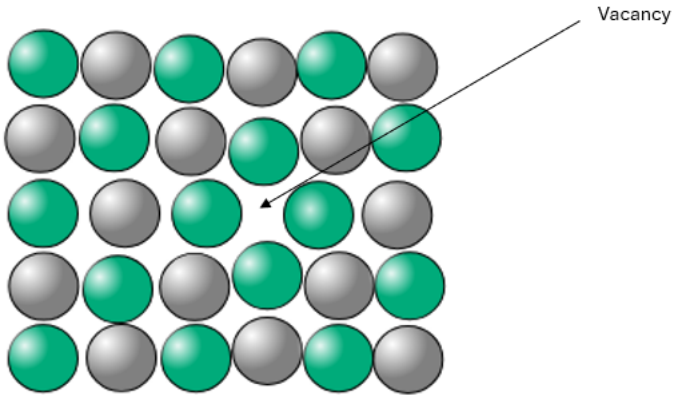

Figure 2.1: Representaion of vacancy in the crystalline solids [10].

2.4.3 Dislocations

A dislocation is a linear or one-dimensional defect within the regular arrangement of atoms or ions in a crystal lattice. There are two types of dislocation, edge and screw dislocation. However, most crystalline materials have both edge and screw dislocation, called mixed dislocations [11]. Plastic deformation corresponds to the motion of large numbers of dislocations. Because of this, the harder it is to move dislocation, the stronger and harder the material is [12].

2.4.4 Slip

Slip can be defined as the process of plastic deformation produced by dislocation movements. Dislocation has

different degrees of ease of motion on different crystallographic planes and directions. Indeed, there are preferred planes and directions in which dislocation motion occurs. This plane and direction are called slip plane and slip direction, respectively, and the combination of these is called slip system. The slip plane has the densest atomic packing. For aluminium, slip plane and slip direction are in {111} and <110> family, respectively [13].

2.4.5 Grain boundary

Grain can be defined as a collection of many small crystals that form during solidification of a polycrystalline specimen. Grains can have a random crystallographic orientation. This results in a boundary between grains, called grain boundaries [14]. The role of grain boundary in the hardening mechanism will be discussed in section 2.5.2.

2.4.6 Phase boundary

Multi-phase materials like alloys have different phases in their structure. Each phase can have its own distinctive physical or chemical characteristics, as it may have different crystal structures and lattices. Boundaries between these phases are called phase boundaries and can be divided into three categories: coherent, semicoherent,

and incoherent. Determining the type of phase boundary depends on the degree of fit of the lattices across the boundary [15].

Coherent boundary is produced when there is a high degree of matching between lattices of two phases. Coherent boundaries have high strain energy, producing a stress field that can impede dislocation movements and, as a result, increase the material's strength [15].

Incoherent boundary is produced when there is no matching between the lattices of two phases across the boundary. Incoherent boundaries have low strain energy and are much less effective in stopping dislocations [15].

Semicoherent boundary shows a partial matching between the lattices of two phases. They have lower strain energy than coherent boundaries but higher than incoherent ones. They contribute to stopping dislocation movements more effectively than incoherent boundaries [15].

2.5 Hardening mechanisms

Hardening processes in material technology involve altering the properties of a material to make it harder, stronger, and more durable. In this section, we go through the following methods that can be applied to aluminium alloys to increase strength:

- Solid-solution hardening
- Grain-size strengthening
- Work hardening
- Precipitation hardening

2.5.1 Solid solution hardening

As mentioned, there is an inverse relationship between dislocation movements and material strength. The more dislocation movement in the material's microstructure is restricted, the harder and stronger the material.[12].
Based on this principle, solid-solution hardening increases materials' tensile and yield strength by adding alloying elements (impurity atoms) substitutionally or interstitially into the solid solution to produce distortions or strain in the parent lattice. The lattice strain field restricts dislocation movements, allowing the material to experience higher strength[16].
For the substitutional type, solute or impurity atoms re-

place or substitute the host atoms in the lattice. If the solute atoms are greater than the host atoms, they will produce compressive strains. Conversely, if the solute atoms are smaller than the host atoms, they will produce tensile strains. Figure 2.2, on the next page, demonstrates a visual representation of the substitutional type. For interstitial solid solutions, impurity atoms fit into the voids or interstices among the host atoms in the lattice. (see Figure 2.3)

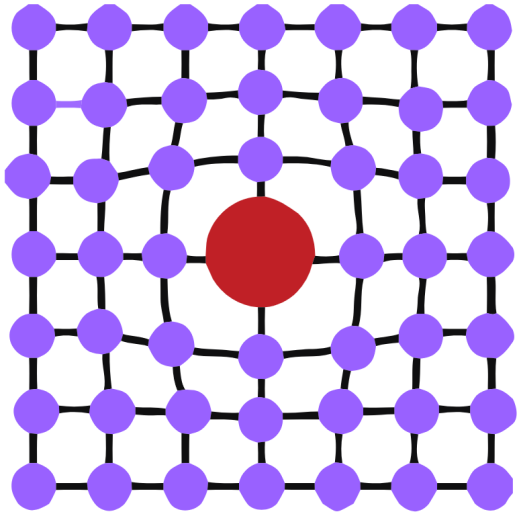

Figure 2.2: A Substitutional Solid Solution[17]

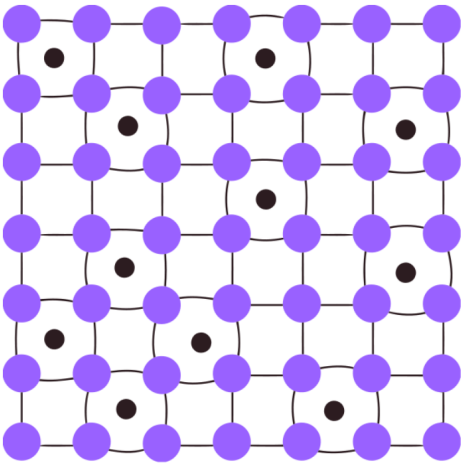

Figure 2.3: An Interstitial Solid Solution[18]

2.5.2 Grain-size hardening

The idea behind grain size hardening is similar to solid solution hardening, as it impedes dislocation movement during plastic deformation. This will be achieved by reducing the grain size (average grain diameter) and increasing the total grain boundary area. As adjacent grains have different crystallographic orientations, boundaries will act as a barrier to dislocation movements, and as a result, the material's strength will increase. Therefore, we can conclude that fine-grained material is stronger because of its greater total grain boundary area than coarse-grained material. The Hall-Petch equation is usually used to calculate yield strength as a function of average grain diameter[19].

$$\sigma_y = \sigma_0 + k_y \cdot d^{-\frac{1}{2}} \tag{1}$$

σ_y is the material's yield stress

σ_0 constant for a particular material

k_y constant for a particular material

d is the average grain diameter

Grain size reduction can be achieved by cold work (cold rolling) and an appropriate heat treatment.

The idea behind grain size hardening is not only limited to grain boundaries. Phase boundaries in alloys can

also impede dislocation movements and increase the material's strength [19].

2.5.3 work hardening

Work hardening is the strengthening of metals by plastic deformation. It is also known as strain hardening or cold working. Deformation is usually induced by rolling, drawing, or forging. In this thesis, cold rolling is used to deform aluminium plates.

Under deformation, when the material reaches the plastic region and the strain is beyond the yield point, more stress is needed to produce additional plastic deformation (more strain). As a result, increasing the degree of deformation causes the material to become stronger [20]. Figure 2.4 (see next page) shows how the material's yield point increases after cold deformation. It shows that more stress is needed to reach the new yield point.
From a microscopic view, cold working increases the density of dislocations by dislocation multiplication or the formation of new dislocations in the material structure. This leads to dislocations lying closer together with a smaller separation distance. As a result, the motion of dislocations becomes more difficult as they hinder themselves from moving; therefore, more stress is needed to deform the material [21].

It should be noted that in the cold working process, as a material's strength increases, the ductility of the material decreases.

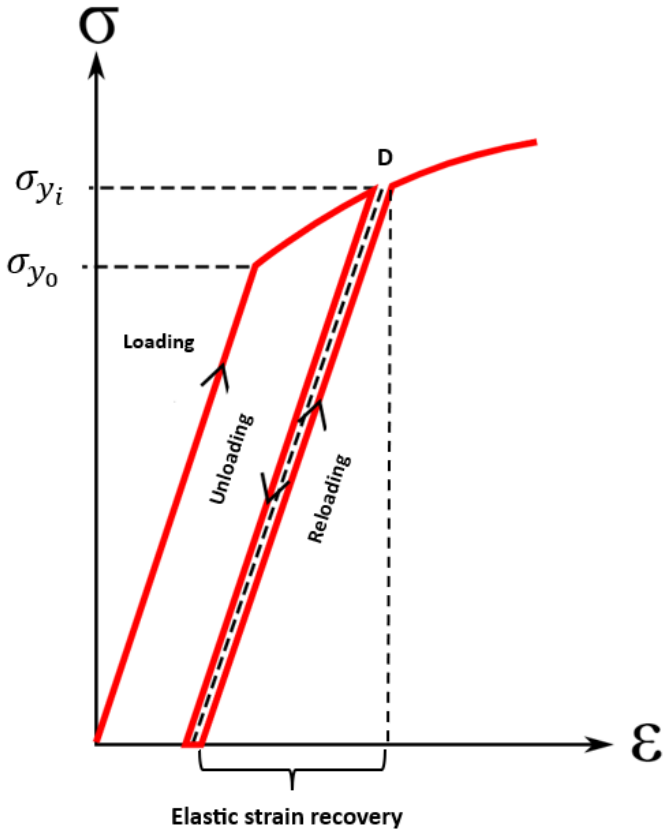

Figure 2.4: Schematic tensile stress– strain diagram showing the phenomena of elastic strain recovery and strain hardening. The initial yield strength is designated as σ_{y0}; σ_{yi} is the yield strength after releasing the load at point D and then upon reloading. (The figure is manipulated by the author. However, the original image can be found here [22]

2.5.4 Precipitaion hardening or age hardening

In the precipitation hardening, numerous small and uniformly dispersed particles will precipitate within the original phase matrix. Because of these precipitated particles, this mechanism is called precipitation hardening. The other term, age hardening, is also used to call this mechanism because the material's strength increases with time, or in other words, as the alloy ages[23].

Again, the idea behind the strengthening is that the precipitated particles will impede dislocation movement as they produce lattice strain and stress field in the matrix. As discussed in Section 2.3, a single-phase solid solution, called α, is formed during solution heat treatment at a hypothetical temperature[2] T_0. At this stage, the elements responsible for the alloy's hardening are entirely dissolved. It should be noted that T_0 should be between the melting eutectic temperature and the solvus line to avoid overheating the alloy [24]. Figure 2.5 shows the approximate value of T_0 in a hypothetical phase diagram.

[2]The actual temperatures are mentioned in the experimental section.

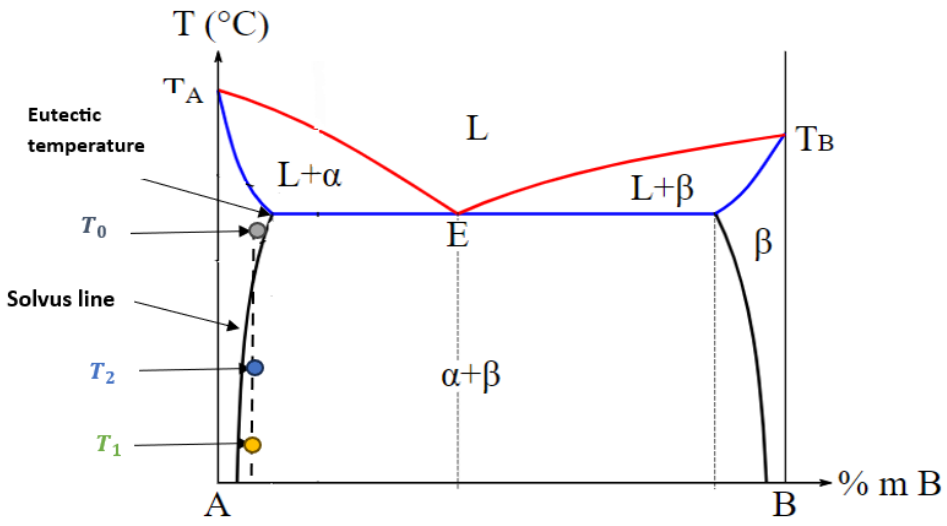

Figure 2.5: Hypothetical phase diagram for a precipitation-hardenable alloy.(The figure is manipulated by the author. However, the original image can be found here[25]

The next stage, quenching the alloy at temperature T_1, takes place. At this stage, the dissolved elements are frozen because of rapid cooling (quenching), and therefore, there is only the solid solution supersaturated phase α. The materials are usually quenched in a medium such as water or air with temperature T_1 (usually room temperature) that can provide rapid cooling.

In the next stage, precipitation heat treatment, the supersaturated solid solution will be heated to intermediate temperature T_2 and held for a long time until a sequence

of meta-stable phase transitions occurs.

Figure 2.6 shows the behaviour for a typical precipitation hardenable alloy.

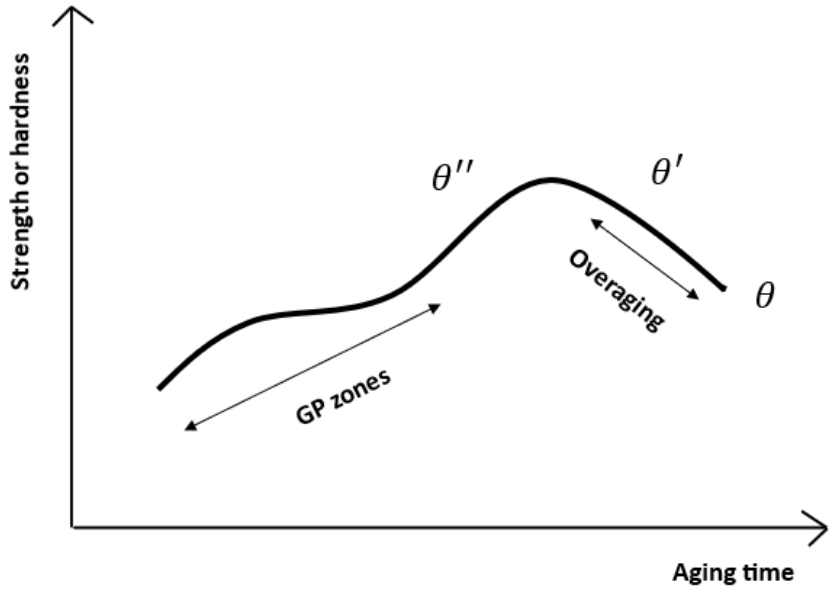

Figure 2.6: Schematic diagram showing hardness as a function of ageing time at a constant temperature during the precipitation heat treatment. (The figure is created by the author)

The meta-stable phases that form during the ageing process are hypothetically called θ'' and θ'. In the initial stages of ageing, elements dissolved in the solid phase form clusters, also known as GP zones. After some time, with more diffusion of the dissolved elements, these zones become greater, forming particles that can be precip-

itated within the crystal structure. The existence of countless of these particles distorts the lattice and impedes the dislocation movement. Figure 2.6 indicates that the highest strength is obtained during the θ'' and θ' phases. If the alloy is maintained at T_2 longer than needed, another phase transition occurs, forming the stable phase, θ. In other words, the alloy is overaged. In this phase, the material loses the strength that it acquires in the θ'' and θ' phases [26]. The goal of ageing is to reach these two phases since countless particles have been precipitated throughout the crystal structure of the alloy.

These particles' character and the degree of hardness and strength of the alloy depend on the temperature T_2 and the ageing time at this temperature.

For an alloy of 6xxx series, the following typical sequence of meta-stable phases holds: Supersaturated solid solution $\rightarrow$ GP zones $\rightarrow$ pre-$\beta''((\mathrm{Al}+\mathrm{Mg})_5\mathrm{Si}_6$) $\rightarrow$ β'' ($\mathrm{Mg}_5\mathrm{Si}_6$, $\mathrm{Al}_3\mathrm{MgSi}_6$) $\rightarrow$ $\beta'(\mathrm{Mg}_9\mathrm{Si}_5)$ $\rightarrow$ $U_1(\mathrm{MgAl}_2\mathrm{Si}_2, \mathrm{MgAl}_4\mathrm{Si}_5)$ $\rightarrow$ $U_2(\mathrm{Mg}_2\mathrm{Al}_4\mathrm{Si}_5, \mathrm{MgAlSi})$ $\rightarrow$ $\beta(\mathrm{Mg}_2\mathrm{Si})$

The coherent metastable phase β', U1 and U2 coexists with β' phase transition [27].

2.6 Effect of Cold rolling on Precipitation hardening

Cold rolling can affect the material's microstructure by inducing defects such as dislocations and vacancies. These effects may significantly influence precipitation kinetics as they can accelerate the ageing response [28] [29]. In addition, they can affect the size and dispersion of the precipitate particles throughout the microstructure during ageing [30] [31]. The alloy system also plays an important role in how cold rolling affects the precipitation process. Alloy 6082 is a family of Al-Mg-Si alloys. How cold rolling affects the precipitation process in this particular type of alloy can be different from the effect of cold rolling on other aluminium alloys such as Al-Cu or Al-Cu-Mg [29].

However, technologies such as a transmission electron microscope (TEM) are required to study the effect of cold rolling on GP zones or precipitate phases such as β' and β'' from a microscopic view. As this thesis will not cover TEM, it will rely on the results of mechanical tests, including hardness tests and tensile tests, to investigate the effect of cold rolling on the precipitation process in the alloy 6082.

2.7 Anisotropy

The dependency of physical properties on the crystallographic direction in a material is termed anisotropy. For example, the elastic modulus can have different values in a crystal structure's [100] and [111] directions[32]. This thesis will study anisotropy due to cold rolling. Cold rolling affects the density of dislocations and the slip system, and this effect can be varied in different planes and directions in the material. Therefore, mechanical tests such as hardness tests and tensile tests will be performed in different planes and directions to see if the mechanical properties of the material are different.

2.8 Texture

Texture can be defined as a preferred orientation of crystalline grains, even though each grain can randomly have different crystallographic orientations. In other words, a material has a texture if grains in the material's structure have a preferential crystallographic orientation. Since texture can affect the material's mechanical properties in different orientations, it implies that the material is anisotropic[32].

Texture can be formed during the solidification of a polycrystalline material or plastic deformation in a cold

work process. For instance, the material will be pressed and drawn between two rolls during cold rolling. Therefore, grains will be forced to have a preferred orientation along the rolling orientation (see Figure 2.7).

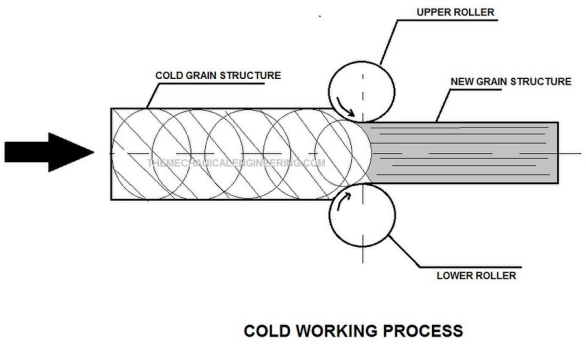

Figure 2.7: Change of grain structure during cold rolling [33]

2.9 Tensile test

Mechanical tests are essential in evaluating, developing and controlling the quality of engineering materials. The tensile test, considered a destructive test, is the most well-known mechanical property test that provides essential information about the material's properties, such as yield strength, tensile strength, Modulus of Elasticity, ductility, toughness and so on [34]. Figure 2.8 shows some of these properties on a typical stress-strain diagram for a ductile material. The diagram for brittle materials usu-

ally does not include plastic deformation because they will be cracked before any plastic deformation.

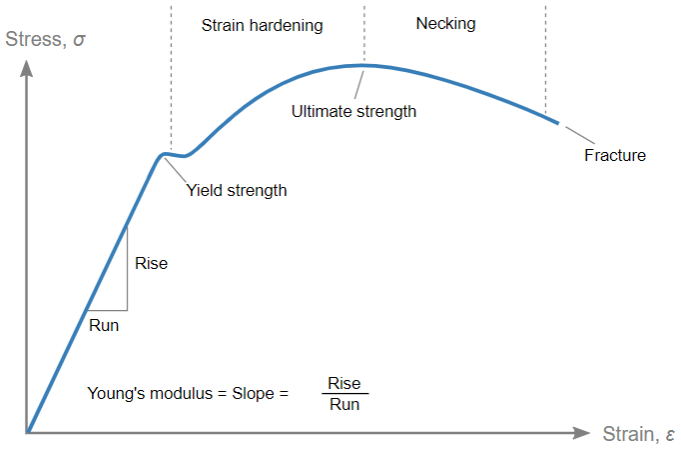

Figure 2.8: Stress-strain curve.The stress unit is in MPa, while strain is measured as a percentage change.[35]

It should be noted that the final plot after testing is given as engineering stress versus engineering strain. Engineering stress and strain are calculated based on the original dimensions of the specimen before deformation. In contrast, true stress and strain consider the actual instantaneous dimensions of the specimen during testing.

Engineering stress:

$$\sigma = \frac{F}{A_0} \tag{2}$$

σ is engineering stress (usually in MPa)

F is the instantaneous load applied perpendicular to the specimen cross-section (N)

A_0 is the original cross-sectional area before any load is applied (m^2)

Engineering strain:

$$\epsilon = \frac{l_i - l_0}{l_0} \tag{3}$$

ϵ is engineering strain

l_0 is the original length before any load is applied

l_i is the instantaneous length

Modulus of elasticity (Hooke's law):

$$\sigma = E\epsilon \tag{4}$$

ϵ is engineering strain

σ is engineering stress (usually in MPa)

E is the Modulus of elasticity (usually in GPa)

Ductility: Ductility is a mechanical property of the material that indicates the degree of deformation the material can endure before fracture during a tensile test. Quantitatively, it is usually measured as either per cent elongation or per cent reduction in area at fracture. The equations below show how to calculate per cent elongation and per cent reduction in area [36].

$$\%EL = \frac{l_f - l_0}{l_0} \times 100 \tag{5}$$

$\%EL$ is percent elongation

l_0 is the original gauge length

l_f is the fracture length

$$\%RA = \frac{A_0 - A_f}{A_0} \times 100 \tag{6}$$

$\%RA$ is percent reduction in area

A_0 is the original cross-sectional area

A_f is the cross-sectional area at the fracture point

Toughness: Toughness is a mechanical property that can be used in several contexts. A common definition is that toughness is the material's ability to absorb energy up to fracture. A stress-strain diagram can be used to measure the toughness of metals, as the area under the stress-strain curve indicates the degree of the material's toughness. Materials with high toughness show high strength and high ductility. [37]

2.10 Hardness test

Hardness is a mechanical property which measures the material's resistance to localized plastic deformation. Several hardness tests have been developed recently, including the Vickers hardness test, Knoop hardness test, Brinell hardness test and Rockwell hardness test [38].
The idea behind all these tests is that a small indenter is forced on the material's surface under controlled conditions, according to the Standards for each hardness test. After that, the depth or size of the created indentation will be measured to calculate the hardness of the material by using a specific formula assigned to each hardness test [38].

2.10.1 Vickers hardness test

Vickers Hardness measurement is a non-destructive way to measure the hardness of a metal. The device uses a diamond pyramid shape, which will be pressed into the sample piece. The hardness is measured in HV (Hardness Vickers) by the Formula below.

$$HV = 0.1891\frac{F}{d^2} \tag{7}$$

F is the applied force in N

d is the arithmetic mean of the two diagonals in mm

Figure 2.9 shows the shape of the pyramid and indentation. In this thesis, the Vickers hardness test has been conducted according to Standard NS-EN ISO 6507-1:2018 [39].

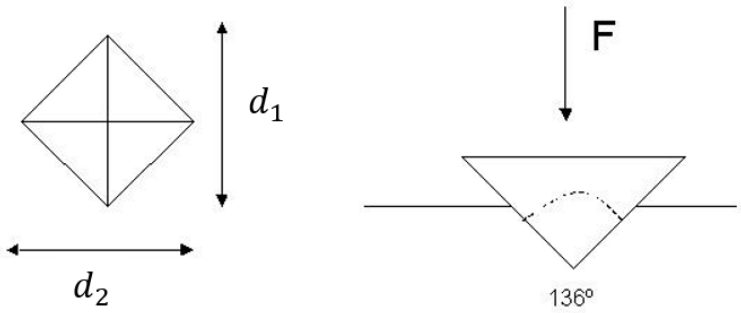

Figure 2.9: Pyramid and indentation.(The figure is manipulated by the author. However, the original image can be found here[40]

2.11 Microscopy

Microscopy examines the characteristics of materials at a microscopic level. It can give us a deep understanding of the relationships between mechanical properties and the microstructure of materials. Microscopy is also a very useful tool for examining the effect of heat treatments and hardening mechanisms on materials. However, it is necessary to prepare the sample's surface to reach a perfect finish for a specific microscopy examination.

2.11.1 Sample preparation

Preparation aims to achieve a proper structure of the specimen under microscopy examination. One of the most common methods is mechanical preparation, which contains grinding and polishing. Usually, the specimen experiences different steps of grinding and polishing to remove any scratches or deformation from the specimen surface. Depending on which material we are working on, a different method for the preparation process can be chosen[41].

Etching can be a chemical or electrolytic process after grinding and polishing procedures. The goal of etching is to enhance surface contrast to visualize the microstructure or microstructure [42]. This thesis will use

electrolytic etching after a series of grinding and polishing steps. The experimental chapter will provide more details.

2.11.2 Optical microscopy

Optical microscopy, or the light microscope, is a traditional technique for studying the microstructure of materials. It uses different lenses with visible light to change the degree of magnification.

2.11.3 Scanning Electron Microscope (SEM)

SEM is one of the most useful tools for investigating the surface of a specimen. It uses an electron gun that shoots a beam of electrons at the specimen. The SEM will detect these electrons and convert them into digital images. In materials science, SEM can detect chemical composition, morphology, topography, and microstructure. Many types of signals are produced when electrons interact with the sample. SEM has different types of detectors to receive these signals. Some signals that can be detected are Characteristic X-rays, Continuum X-rays, Fluorescent X-rays, secondary electrons (SE), backscattered electrons (BSE), and Auger electrons [43].

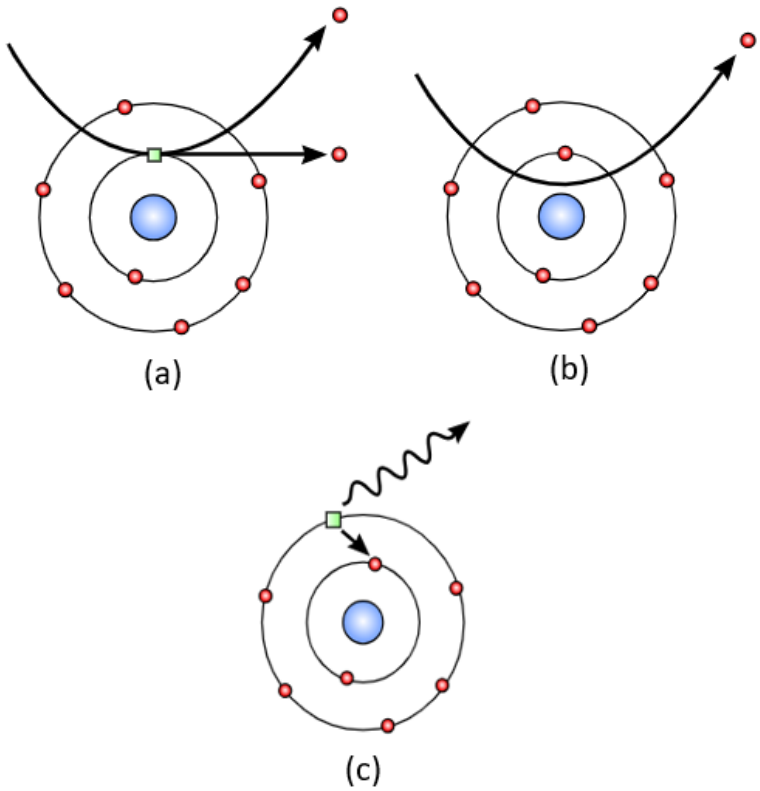

Figure 2.10: A schematic representation of (a) Secondary electrons SE, (b) Backscatter electrons BSE, (c) X-rays.[44]

Secondary electrons: Secondary electrons (SEs) are low-energy electrons due to inelastic collision with atoms. SEs can be used to examine the specimen's cross-section after tensile tests to determine whether the specimen is brittle or ductile. SE has a higher resolution than BSE [43].

Backscattered electrons: Backscattered electrons have higher energy than SEs because their collisions with atoms are elastic. Backscattered electrons are helpful to show phase distribution in the sample [43].

X-rays: X-rays are high-energy photons that emit from the collision of electron beam with atoms. The most important type is Characteristic X-rays, which the Energy Dispersive X-ray (EDS) technique will detect [43].

2.11.4 Energy Dispersive X-Ray spectroscopy (EDS)

EDS, or Energy Dispersive X-ray spectroscopy, is a technique for determining different materials' elements or chemical composition. A detector detects characteristic X-rays radiated by the interaction of incident electrons. When the high-energy electron beam hits a sample, it kicks out inner electrons and creates a vacancy in the electron orbital of the inner shell. Other electrons with higher electron levels fill these vacancies, releasing energy as characteristic X-rays.

Characteristic X-rays have a specific energy value for each element. This energy value acts as an identifier for each element of the sample (qualitative analysis), and the intensity of the characteristic X-rays is a measurement to determine the content of each element (quantitative analysis) [45]. The result will be mapped on a coordinate axis

like Figure 2.11. The X-axis indicates X-ray energy, and the Y-axis indicates relative intensity or counts.

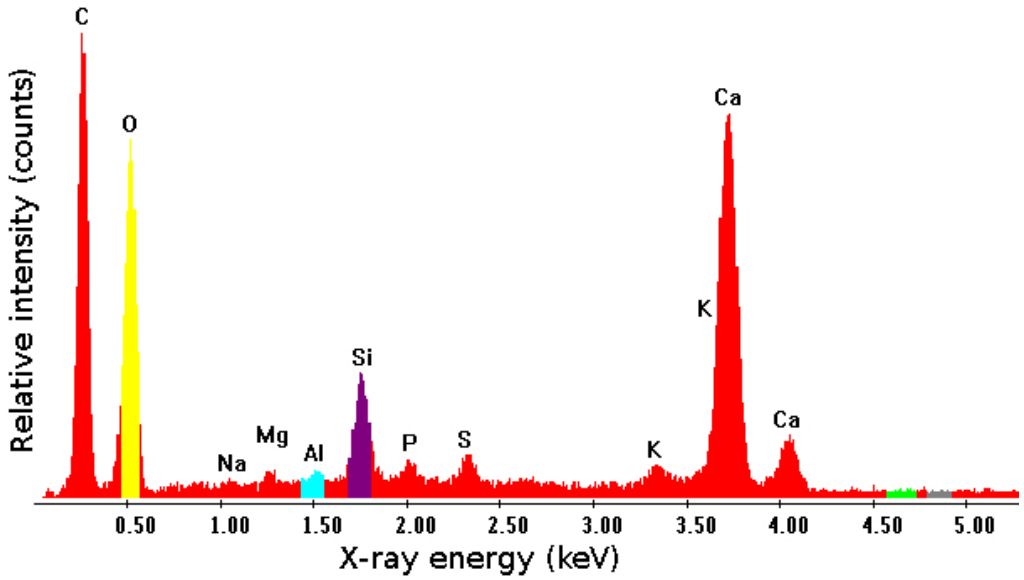

Figure 2.11: Energy-dispersive X-ray spectroscopy showing qualitatively the elemental composition of a poppy seed.[46]

2.11.5 Electron Backscatter Diffraction (EBSD)

EBSD, or Electron Backscatter Diffraction, is a technique to analyze and visualize crystal structure and crystal orientation. EBSD technique collects Backscatter electrons (BSE) that satisfy Bragg's law as they exit the specimen over a large solid angle, which forms diffraction patterns made up of Kikuchi bands (see Figure 2.12). These patterns will be analyzed to determine the crystalline structure and orientation [47]. EBSD can also determine local

texture and grain orientation, which might be present after cold rolling [48].

Bragg's law: A general relationship among x-ray (or electron in EBSD) wavelength, interatomic spacing, and diffraction angle for constructive interference.

$$2dsin\theta = n\lambda \tag{8}$$

d is the spacing between the crystal lattice planes.

θ is the angle of incidence of the X-rays or waves onto the crystal lattice planes.

n is an integer representing the order of the diffraction peak.

λ is the wavelength of the incident waves.

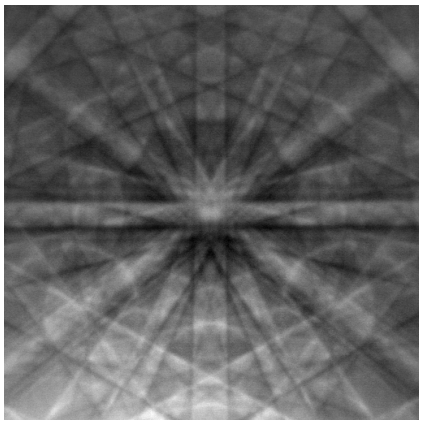

Figure 2.12: A typical EBSD pattern from a single crystal of Silicon consists of straight, bright bands called Kikuchi bands.[49]

3 Exprimental

The project started by receiving a plate of alloy 6082 with a dimension of 700x500x5 mm at the initial state. Table 3.1 represents the chemical composition of this alloy.

Table 3.1: Chemical composition of alloy 6082

Alloy	**Si**	**Fe**	**Cu**	**Mn**	**Cr**	**Ti**	**Mg**	**Zn**
6082	0.9	0.15	0.005	0.52	0.15	-	0.61	0.03

The plate experienced hot working in advance and had an already rolling direction along the length of the plate(see Figure 3.1). The cold rolling in this thesis was performed in the same direction.

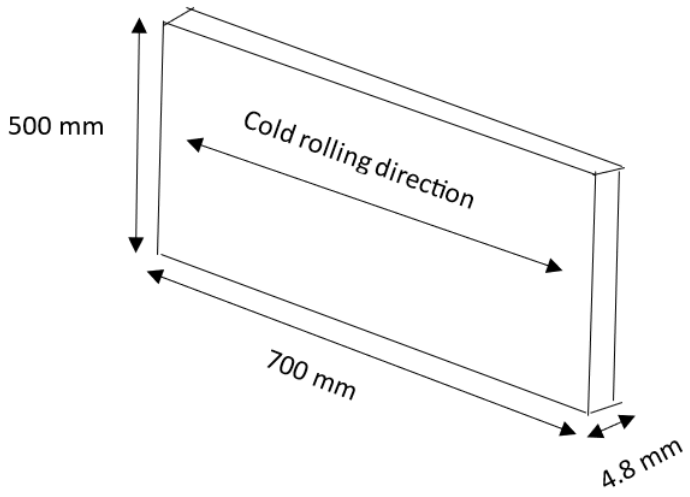

Figure 3.1: Plate's dimension and cold rolling direction at the initial state.

3.1 Sample Preparation

The process of preparation started by cutting the plate, using a circle saw, into seven smaller plates of different sizes. Figure 3.2 shows a schematic of the plates and their dimensions.

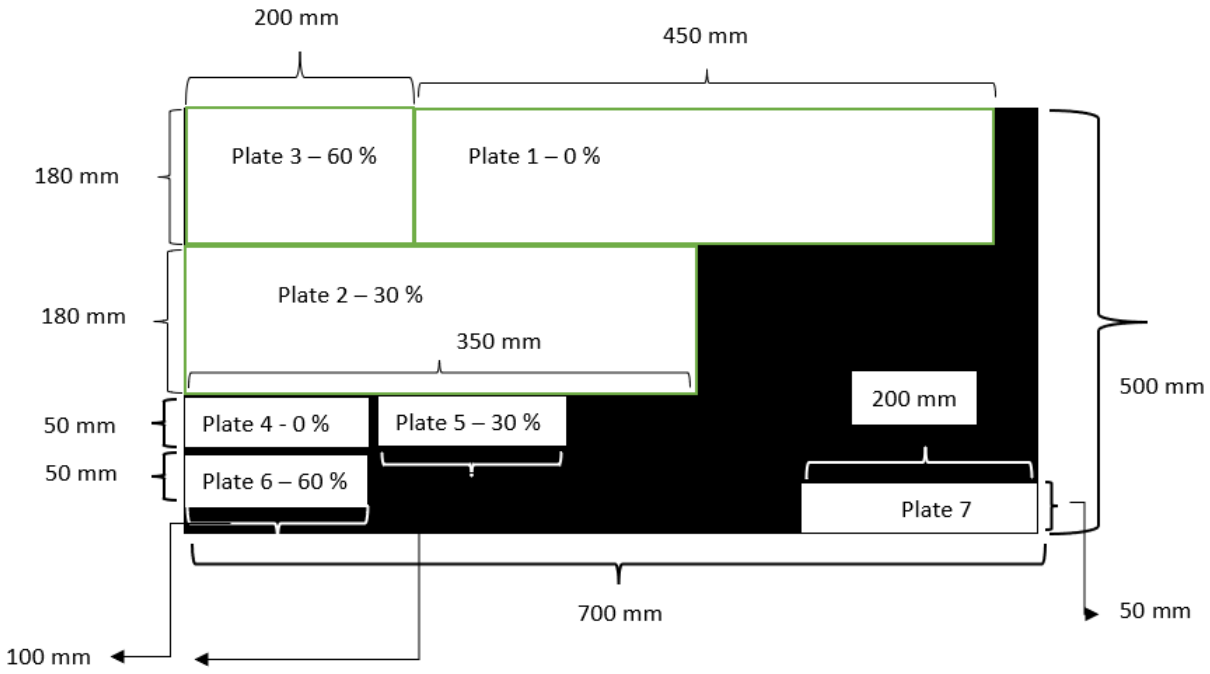

Figure 3.2: An overview of cut plates and their dimensions

The percentage beside the number of plates indicates how much they would be deformed during the cold rolling process.

The first step was to ensure the material could endure cold rolling for 60 per cent deformation without cracks.

Plate 7 was utilized to perform this test, and the result was satisfactory.

Plates 1, 2, and 3 were cut to undergo solution heat treatment (SHT), cold rolling, and artificial ageing. In return, plates 4, 5 and 6 were cut to experience only SHT and cold rolling. These plates were left at room temperature to experience natural ageing.

3.2 Heat treatments

Figure 3.3, on the next page, shows the process of two heat treatments performed in this thesis. The first heat treatment (solution heat treatment) occurs at 540°C for 1 hour, and the second heat treatment (artificial ageing) takes place at 180°C for 8 hours. Quenching occurs in water at room temperature right after solution heat treatment. After artificial ageing, the material is exposed to air to cool to room temperature. A Nabertherm furnace was used to conduct both heat treatments.

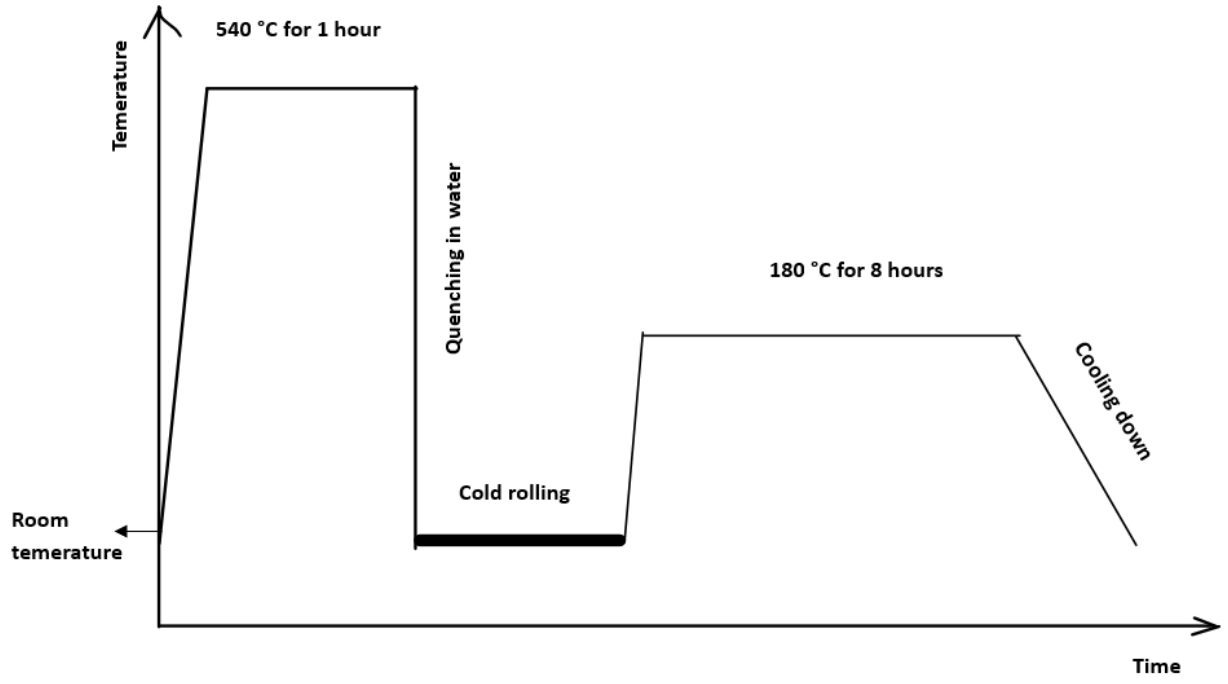

Figure 3.3: An overview of the entire process performed in this thesis. The temperature and time are shown above each stage.

3.2.1 Heat treatment of plates 1, 2 and 3

Plates 1, 2 and 3 (refer to Figure 3.2) underwent both solution heat treatment and artificial ageing. Initially, the furnace was set to 540°C to preheat. Once the furnace reached 540°C, all three plates were placed on top of each other inside the furnace. Because of the opening of the furnace, the furnace lost its temperature to some degrees. Therefore, the measuring time started when the temper-

ature in the furnace reached 540°C and stabilized again. No gap was placed between the plates because bending in the plates at high temperatures was possible. On the other hand, since aluminium has high thermal conductivity, it was assumed that the temperature could be the same in all three plates.

After one hour, the plates were quenched in water, and cold rolling was started. Simultaneously, the furnace was cooled to close to room temperature using an external cooling fan during the cold rolling process. This was necessary since changing the temperature from 540°C to 180°C at once was impossible. Once the furnace cooled sufficiently, it was again set to 180°C to preheat until the cold rolling process was performed thoroughly. After the cold rolling was completed, the plates were placed back in the furnace and left for 8 hours. It took 45 minutes from the time the plates were quenched until they were put back in the furnace for artificial ageing. After artificial ageing, the plates were exposed to the air to cool to room temperature. Some samples were extracted from these plates for conducting hardness, microscopy and tensile tests after artificial ageing. The number and dimensions of these samples will be given in the following sections.

3.2.2 Heat treatment of plates 4, 5 and 6

Plates 4, 5 and 6 (refer to Figure 3.2) experienced only solution heat treatment. The process was the same as the process done for plates 1, 2 and 3.

After one hour, the plates were quenched in water, and cold rolling deformation was performed. After the cold rolling process, some samples were extracted from these plates to conduct hardness tests at different time intervals. The reason for this was to study the effect of natural ageing on the hardness of the material.

3.3 Cold work

In this thesis, three degrees of thickness reduction, including 0, 30 and 60 per cent, were conducted on the plates by the Schmitz cold rolling machine in the Uis workshop (see Figure 3.4 on the next page).

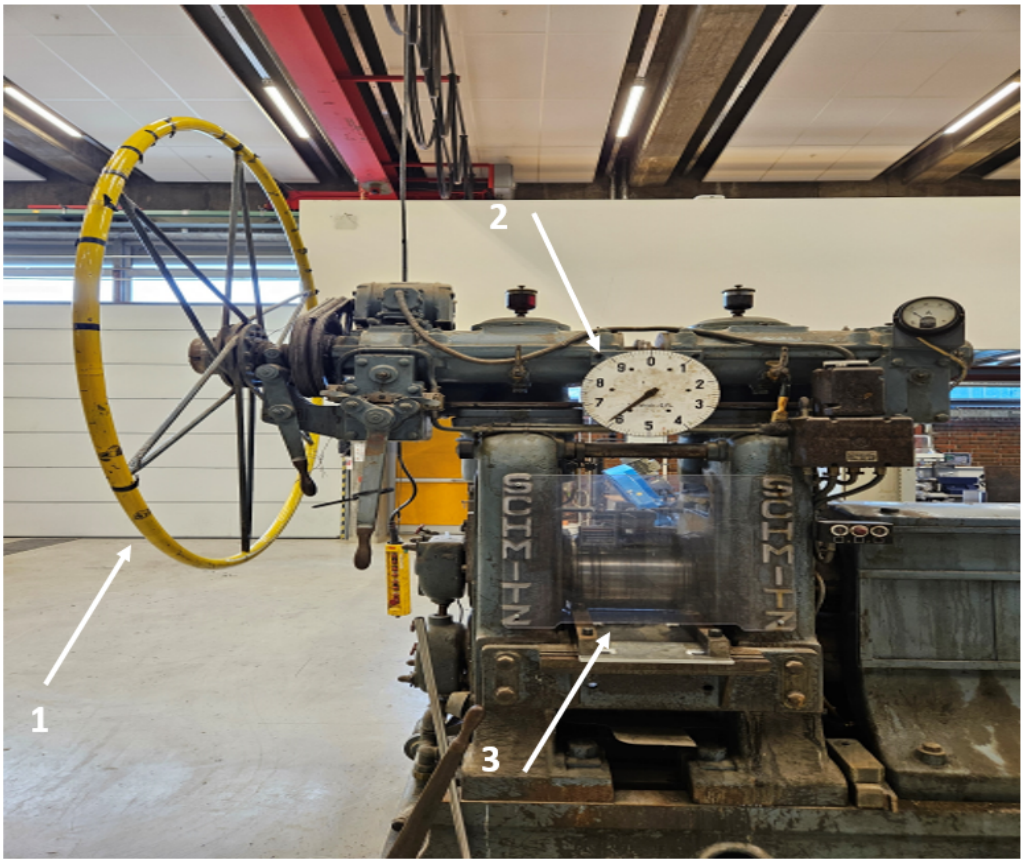

Figure 3.4: Cold rolling machine used in this thesis. 1: The yellow wheel adjusts the desired thickness value at each step. 2: The clock hand shows the value adjusted by the wheel. 3: The rollers that the material is passed between.

The cold rolling process occurred sequentially with around 11-12 per cent thickness reduction at each step, based on the previous thickness value. Table 3.2 indicates the calculations of the theoretical value of the thickness at each step. However, it was difficult to precisely achieve the theoretical values because adjusting the thickness by a clock hand may have a slight error. In addition, it also seemed that the surface of the machine's rollers was slightly worn and misaligned. Table 3.3 shows the actual per cent deformation and the real thickness value of each plate at each step.

Table 3.2: Theoretical values of plate's thickness (mm) at each step. All values are rounded to two decimal places. The thickness of 30% and 60% plates are reduced with 11% and 12% thickness reduction at each step, respectively.

0 %	5.00
30 %	5.00 → 4.45 → 3.96 → 3.52
60 %	5.00 → 4.40 → 3.90 → 3.43 → 3.00 → 2.64 → 2.32 → 2.00

Table 3.3: Actual values of plate's thickness (mm) at each step. All values are rounded to two decimal places.

plate 1- 0 %	5.00
plate 2- 34%	5.00 → 4.40 → 3.95 → 3.30
plate 3- 59%	5.00 → 4.40 → 3.90 → 3.45 → 3.05 → 2.65 → 2.35 → 2.05
plate 4- 0 %	5.00
plate 5- 33%	5.00 → 4.15 → 3.80 → 3.35
plate 6- 59%	5.00 → 4.10 → 3.80 → 3.40 → 3.00 → 2.60 → 2.33 → 2.05

A digital calliper was used to measure the thickness at each step. It should be noted that the plates were turned around randomly at each step to obtain an evenly distributed deformation. As a rule of thumb, once the plate is bent due to rolling, it should not be turned around for the next step. Instead, it should be rolled the same way as the previous step, and then it can be turned around and rolled again for the next step.

3.4 Hardness test

The main goal of this thesis is to study the effect of the combination of cold work and precipitation hardening on the strength of the aluminium alloy 6082. To achieve this goal, various hardness tests were performed on the material. In addition, anisotropy was also studied by testing hardness in different planes of the plate.
In total, seven samples were cut from the plates and tested. All hardness tests were performed by InnovaTest masking in the workshop at the University of Stavanger. Also, since mounting the samples to perform the hardness test had to be done at 180°C for five minutes, it was decided to prepare the samples manually to prevent the possible high-temperature effect on the material's hardness. For this purpose, all samples were ground with #500 paper for about 3 to 5 minutes to obtain a rela-

tively flat surface. Since the surface of the samples was not polished, the hardness was measured by the Vickers hardness test with a relatively high weight of 10 kilograms.

To make the result understandable, the table below indicates a set of abbreviations for the samples and the planes based on the operations they experienced.

Table 3.4: Name of the hardness test samples

IS	Sample at initial state without any cold deformation and heat treatments.
0-AA	0 percent deformed and artificially aged.
30-AA	30 percent deformed and artificially aged.
60-AA	60 percent deformed and artificially aged.
0-NA	0 percent deformed and naturally aged.
30-NA	30 percent deformed and naturally aged.
60-NA	60 percent deformed and naturally aged.
PCR	Perpendicular to the cold rolling direction.
ACR	Along cold rolling direction

3.4.1 Hardness test - Artificial ageing

Three small samples, namely 0-AA, 30-AA and 60-AA, from plates 1, 2 and 3 (refer to Figure 3.2) were extracted to test hardness after artificial ageing. From plate 7, one sample (IS) was cut to test hardness at the initial state before any cold deformation and heat treatments. The hardness test was performed on two sides of these samples to study the anisotropy due to cold rolling.

Figure 3.5 illustrates which sides of the sample have been tested.

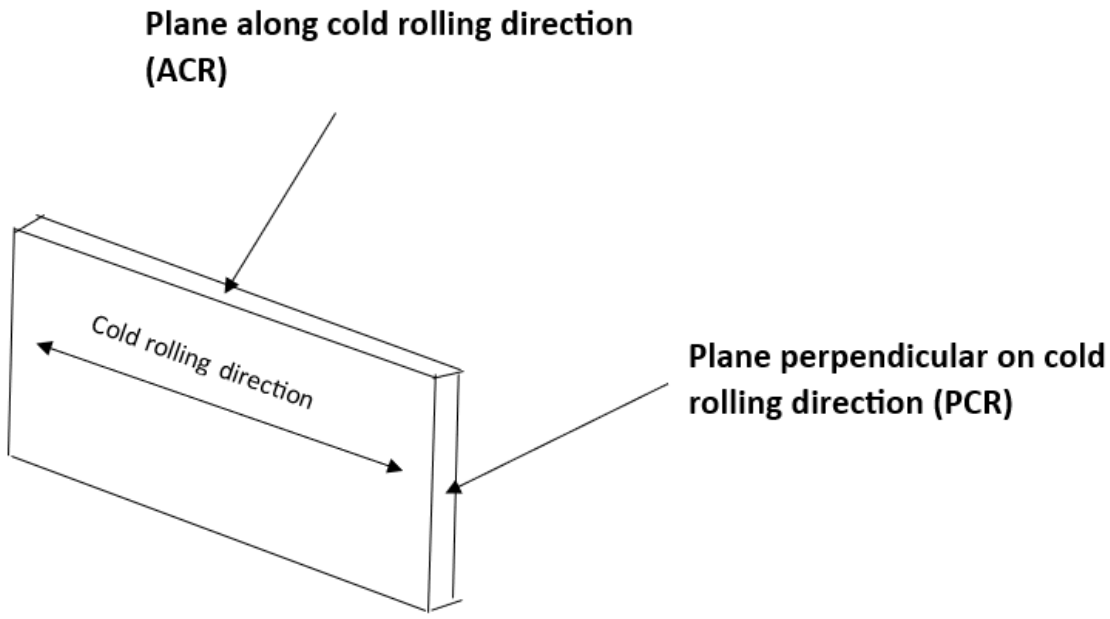

Figure 3.5: Hardness test sample and the planes where the hardness test was conducted.

3.4.2 Hardness test - Natural ageing

Three small samples, namely 0-NA, 30-NA and 60-NA, from plates 4, 5 and 6 (refer to Figure 3.2) were extracted to investigate the effect of natural ageing on the material's hardness. The hardness test for these samples was performed only on the plane PCR.

The hardness test for samples 0-NA, 30-NA and 60-NA was conducted at different intervals to study how the material's hardness changes as the time of natural ageing increases. The table below shows the time intervals in which the hardness test was conducted on these samples.

Table 3.5: Table illustrates the time intervals in which the hardness test was conducted on samples 0-NA, 30-NA and 60-NA. The reference time is after solution heat treatment.

Hardness test	**Time**
Test 1	after 1 h
Test 2	after 3 h
Test 3	after 7.5 h
Test 4	after one day
Test 5	after two days
Test 6	after one week
Test 7	after two weeks

3.5 Tensile test

A total of 24 specimens were prepared for tensile testing. 6 specimens were extracted from each of plates 1, 2 and 3 (in total, 18 specimens) so that three specimens were along the cold rolling direction and the other three were perpendicular to the cold rolling direction. In the same way, six specimens were extracted from the rest of the initial plate to perform the tensile test at the initial state of the material. All specimens were machined by Mazak CNC according to ASTM standard 2004 [50]. Figure 3.6 illustrates the shape and dimensions of the specimens. It should be noted that the thickness of the specimens was different due to 0 (5 mm), 30 (3.30-3.35 mm) and 60 (2.05 mm) per cent deformation.

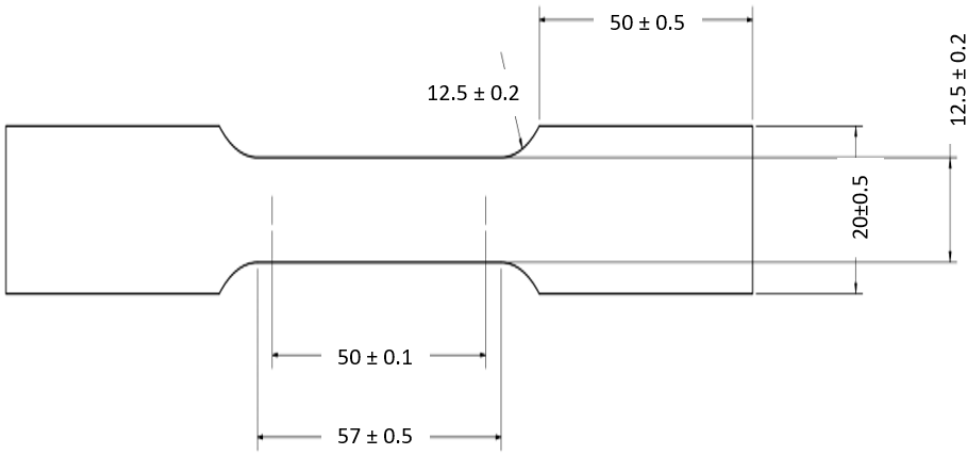

Figure 3.6: Shape and dimensions of the tensile test sample. All measurments are in mm.

All tensile tests were conducted on an Instron 5985 testing machine in the Uis workshop. According to test method A in ISO standard NS-EN ISO 6892-1:2016 [51], a constant strain rate of 0.00025 $\frac{1}{s}$ was chosen during the whole process of the tensile test. Since the Instron machine's extensometer did not work, an external extensometer was used instead. Unfortunately, during the tensile testing process, we faced two serious challenges. The first challenge was that the testing machine clamps could not hold some specimens' heads stably without any slippage. Slipping or sliding of the specimen caused the diagram drawn by the software to have some noise. The second challenge was that installing the extensometer on the specimen stably and without any sliding was not entirely possible, and it had occasional slipping during the tensile test process for a few of the samples. Because of these two challenges, All diagrams were redrawn using raw data produced by the test machine. Using Formula 5, the elongation values were measured by dividing all the displacement values (produced by the test machine) by the initial length of the reduced section of the specimen.

To make the result understandable, Table 3.6 indicates a set of abbreviations for the tensile test specimens.

Table 3.6: Name of the tensile test specimens

A_IS	Along cold rolling direction at initial state.
P_IS	Perpendicular to cold rolling direction at initial state.
A_0	Along cold rolling direction, 0 percent deformed and artificially aged.
P_0	Perpendicular to cold rolling direction, 0 percent deformed and artificially aged.
A_30	Along cold rolling direction, 30 percent deformed and artificially aged.
P_30	Perpendicular to cold rolling direction, 30 percent deformed and artificially aged.
A_60	Along cold rolling direction, 60 percent deformed and artificially aged.
P_60	Perpendicular to cold rolling direction, 60 percent deformed and artificially aged.
PCR	Perpendicular to cold rolling
ACR	Along cold rolling

3.6 Microscopy

3.6.1 Sample preparation for optical microscopy

Grinding and polishing steps were conducted on the material's surface before optical microscopy. Table 3.7 indicates the steps utilized to prepare the samples for optical microscopy. All preparation steps were conducted on the Struers TegraPol-35 automatic polisher.

Table 3.7: Preparation steps for optical microscopy

Steps	1	2	3	4
Surface	SiC-Foil	MD-Dac	MD-Mol	MD-Nap
Grain size	SiC #320	$9\mu m$	$3\mu m$	$1\mu m$
Suspension	water	DiaPro Allegro 9	DiaPro Mol	DiaPro Nap-B
Rotational speed (rpm)	300	150	150	150
Force [N] / Specimen	30	40	25	15
Time [min]	1.5	6	2	2

After the last polishing step, an electrolytic etching was used to enhance surface contrast and observe the grain

and grain boundaries under optical microscopy. The properties of the electrolytic etching are presented in Table 3.8.

Table 3.8: Properties of Electrolytic etching

Electrolyte	**Temp**	**Voltage**	**Flow rate**	**Time (s)**
Barkers	25°C	25V	11	120

Since electric connectivity between the top and down of the mounted sample was required during etching, all samples for optical microscopy were mounted by combining two resins, ConduFast and MultiFast. Condufast was used to cover the top of the sample since it is conductive, and Mutltifast covered the rest. All samples were cut using a Discotom 10 machine with a height of 15 mm. The amount of Condufast and Multifast used was about 1 ml and 15 ml, respectively. The mounting process was performed by using a Struers CitoPress-30 hot mounting machine. The process started by mounting the samples at 180°C for 3 minutes and ended by cooling down the mounted sample for 2 minutes.

3.6.2 Sample preparation for Scanning electron microscope (SEM)

The grinding and polishing steps for SEM are presented in table 3.9.

Table 3.9: Preparation steps for SEM

Steps	1	2	3	4	5
Surface	SiC-Foil	MD-Dac	MD-Mol	MD-Nap	MD-Chem
Grain size	SiC #320	$9\mu m$	$3\mu m$	$1\mu m$	$0.25\mu m$
Suspension	water	Allegro 9	Mol	Nap-B	OP-S
Rotational speed (rpm)	300	150	150	150	150
Force [N] / Specimen	30	40	25	15	10
Time [min]	1.5	6	2	2	3

All samples were embedded in Polyfast resin, which is conductive and required for Scanning electron microscopy. The amount of Polyfast used was about 15 ml. The mounting process was performed by using a Struers CitoPress-30 hot mounting machine. The process started by mounting the samples at 180°C for 3 minutes and ended by cooling down the mounted sample for 2 minutes.

3.6.3 Optical microscopy

Both planes, ACR and PCR (see Figure 3.7 on the next page), were studied under optical microscopy. Six samples with 0 %, 30 % and 60 % deformation and artificially aged were prepared (three samples for each of the planes ACR and PCR) following the procedure explained in Ta-

ble 3.7. An optical microscope called Olympus GX53 was used to study the samples' microstructure.

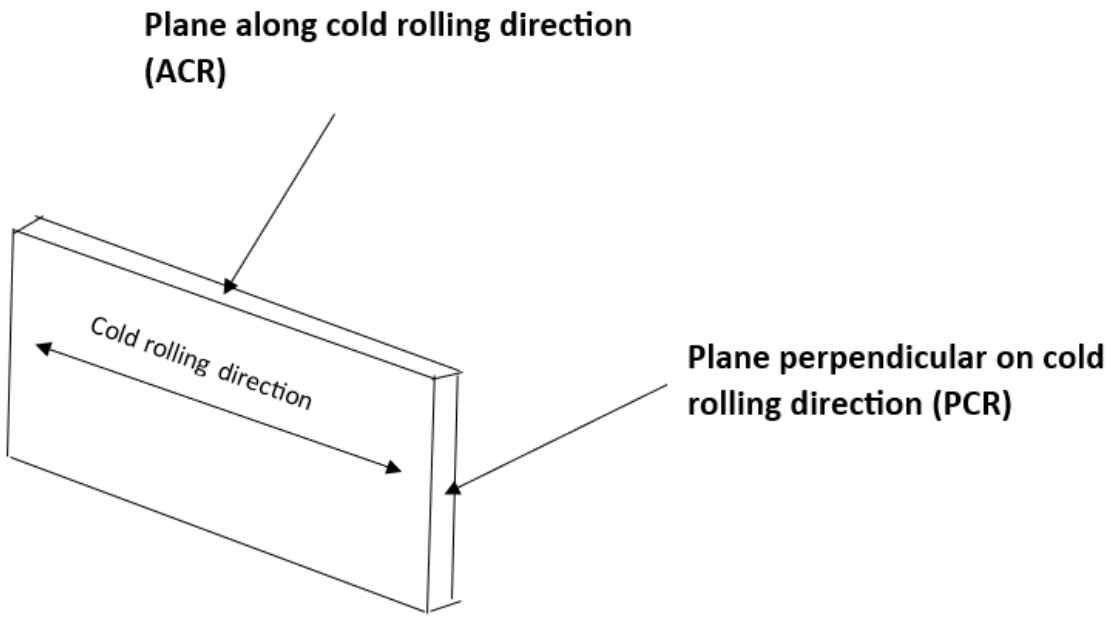

Figure 3.7: Illustration of planes ACR and PCR.

3.6.4 Scanning electron microscopy

Only the ACR plane was studied under Scanning Electron Microscope. Three samples with 0 %, 30 % and 60 % deformation were cut (after artificial ageing) and prepared following the procedure explained in Table 3.9. After taking some pictures of these samples, many unknown white particles were observed throughout the microstructure. Therefore, two other samples were prepared before and after the solution heat treatment to investigate what these particles were and when they were created.

During several lab sessions using a Zeiss Supra 35VP Scanning electron microscope, secondary electrons (SE), backscatter electrons (BSE), EDS analysis, and EBSD were conducted. SEs were used to focus on the microstructure, which was much easier than using BSEs. BSEs were used to take some ordinary pictures of the microstructures. As mentioned, many white particles were observed throughout the microstructure; therefore, an EDS analysis was used to investigate the elements of these particles. EBSD was used to study the grain orientation, texture and grain size of the samples 0 %, 30 % and 60 %. The grain size was measured using the linear intercept method. In this method, many lines are randomly drawn through the photomicrograph, showing the material's grain structure. Afterwards, the num-

ber of grain boundaries intersected by these lines will be counted. Considering P as the sum of the total number of intersections and Ł$_T$ as the total length of all the lines, the mean intercept length $\overline{\mathscr{L}}$, representing the average grain diameter, will be calculated using Formula 9 [52].

$$\overline{\mathscr{L}} = \frac{L_T}{PM} \tag{9}$$

M is the magnification.

NORDIF and EDAX OIM software were also used to collect data and index to produce images using EBSD.

4 Results

4.1 Hardness

This section presents the results of all hardness tests. To make the results clearer and more understandable, it is divided into four subsections.

4.1.1 Cold work and Artificial ageing

Table 4.1 represents the average and standard deviation values of five indentations of the hardness test conducted on the plane PCR (refer to Figure 3.5) for samples IS, 0-AA, 30-AA and 60-AA (refer to Table 3.4 to review the definition of the abbreviations). To see all values of indentations, refer to Appendix A.

Table 4.1: Results of Vickers hardness test (HV10) conducted on the plane perpendicular to cold rolling direction (PCR).

Samples	IS	0-AA	30-AA	60-AA
Average	53.92	99.66	122.16	126.04
STD	0.83	2.78	1.57	0.52

Referring to table 4.1, it is observable that precipitation hardening (by artificial ageing) increased the hardness of the material significantly. By comparing sample IS and 0-AA, the hardness of the material has been increased by about 46 HV10, equivalent to an increase of

around 85 % just due to precipitation hardening. Similarly, comparing sample IS and samples 30-AA and 60-AA, we can observe that the combination of cold work and precipitation hardening has a much higher impact on increasing the hardness than performing only precipitation hardening. This impact equals a 126% increase due to 30% deformation along with artificial ageing and a 134% increase due to 60% deformation along with artificial ageing, compared to the initial state. In addition, by comparing sample 30-AA with sample 60-AA, we can observe that although the amount of cold deformation is enhanced from 30% to 60%, the difference in the hardness increase of the material for these two samples is just 6%. Figure 4.1, on the next page, also illustrates the average hardness of each sample by a bar plot to observe the difference between them visually.

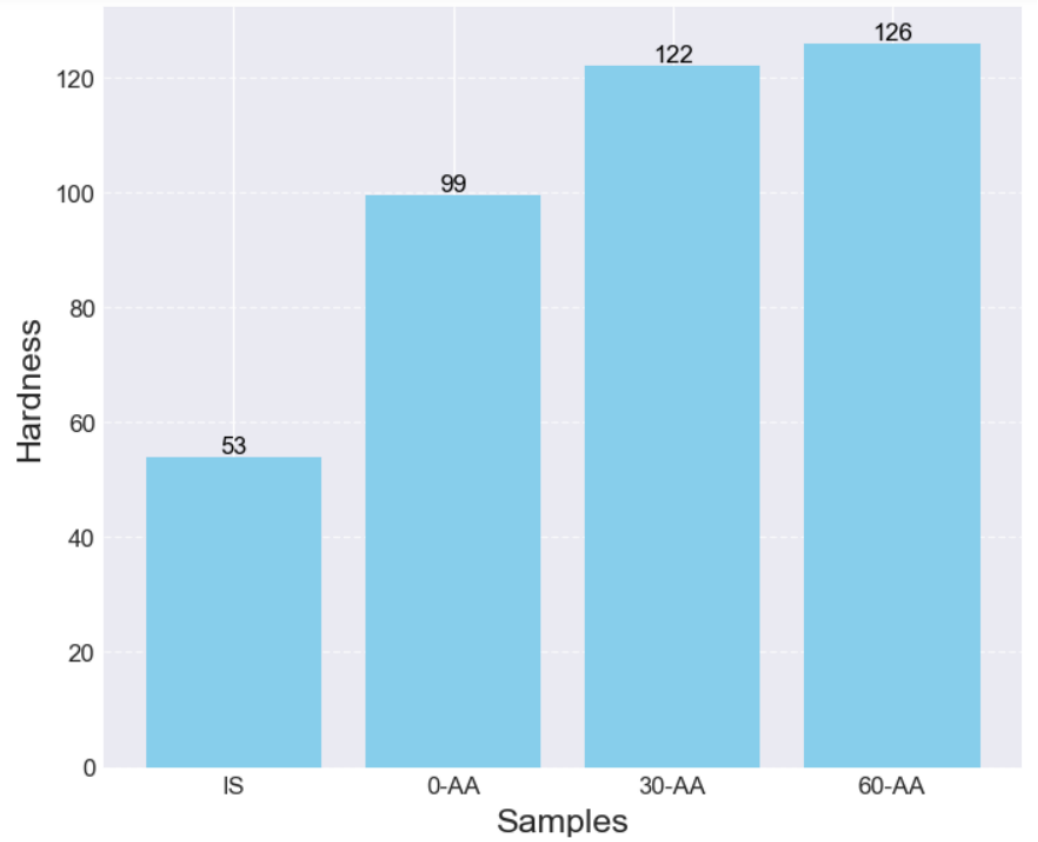

Figure 4.1: The bar plot illustrates the hardness value (conducted on plane PCR) of samples IS, 0-AA, 30-AA and 60-AA.

Table 4.2: Results of Vickers hardness test (HV10) conducted on the plane along cold rolling direction (ACR).

Samples	IS	0-AA	30-AA	60-AA
Average	54.82	101.98	127.30	132.80
STD	0.54	1.43	1.61	1.33

Table 4.2 shows the hardness test result on the plane ACR. The hardness test on this plane aimed to study the possible anisotropy in the material resulting from cold rolling. By comparing Tables 4.1 and 4.2, it can be found that the hardness of all samples, including IS, 0-AA, 30-AA, and 60-AA is higher in the ACR plane as compared to the PCR plane by 1.67%, 2.32%, 4.2% and 5.36%, respectively. Figure 4.2 (see next page) shows the difference in hardness in two planes for each sample using a bar plot. The presence or absence of anisotropy will be discussed in the discussion chapter, section 5.1.3.

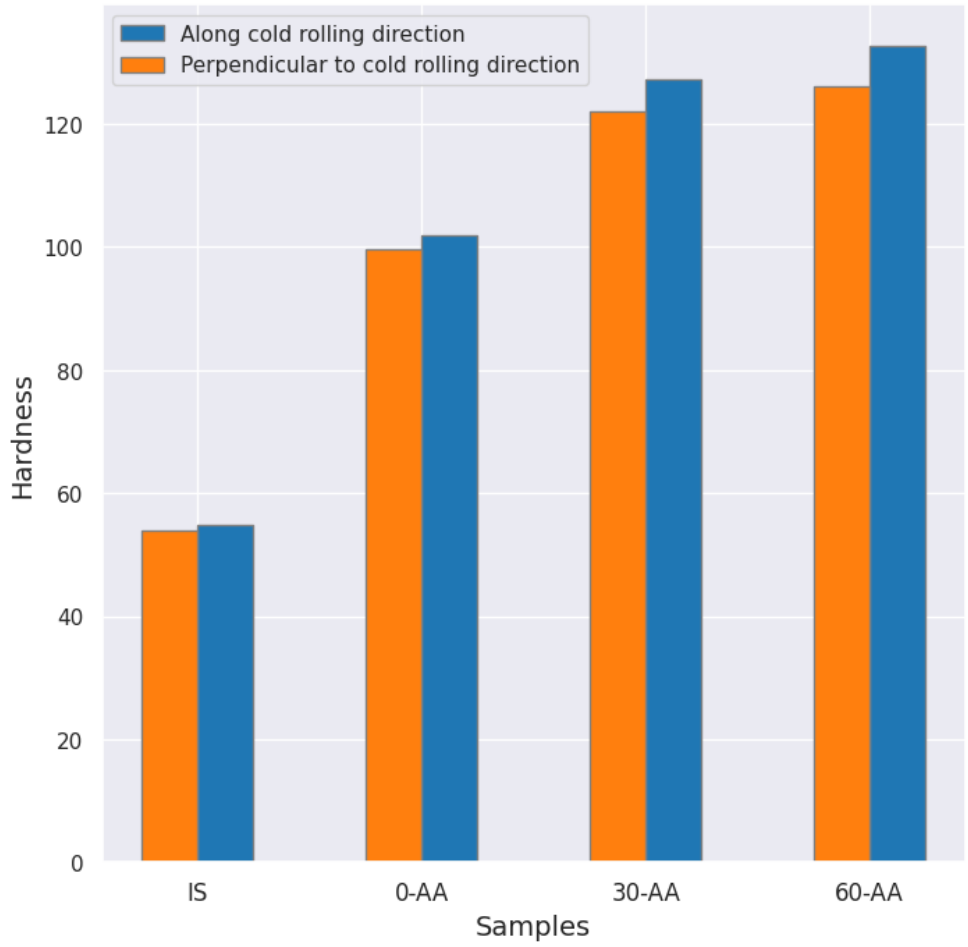

Figure 4.2: The bar plot illustrates the hardness value of samples 0-AA, 30-AA and 60-AA in two different planes (ACR and PCR).

4.1.2 Cold work and Natural ageing

Several hardness tests were conducted on samples 0-NA, 30-NA and 60-NA in different intervals to see the changes in the hardness. Table 4.3 below shows the average and STD values of the hardness for these samples at various intervals. The sample IS is also added to the table to see the effect of natural ageing more clearly. In addition, Figure 4.3 shows a diagram of the development of the samples' hardness over time.

Table 4.3: Results of Vickers hardness test (HV10) conducted on the plane perpendicular to cold rolling direction (PCR). The reference time is after solution heat treatment.

Samples	IS	0-NA	30-NA	60-NA
after 1-h	avg=53.92 std=0.83	avg=66.83 std=0.55	avg=91.36 std=1.17	avg=103.80 std=1.06
after 3-h	avg=53.92 std=0.83	avg=72.18 std=1.10	avg=93.20 std=0.87	avg=107.98 std=1.26
after 7.5-h	avg=53.92 std=0.83	avg=78.23 std=0.86	avg=96.42 std=1.49	avg=110.56 std=0.95
after 1-d	avg=53.92 std=0.83	avg=80.68 std=0.62	avg=101.47 std=1.42	avg=114.32 std=2.33
after 2-d	avg=53.92 std=0.83	avg=83.57 std=1.88	avg=102.05 std=1.65	avg=115.44 std=1.05
after 1-w	avg=53.92 std=0.83	avg=88.32 std=1.38	avg=105.24 std=1.21	avg=117.46 std=1.25
after 2-w	avg=53.92 std=0.83	avg=89.20 std=0.97	avg=105.38 std=1.53	avg=117.56 std=1.03

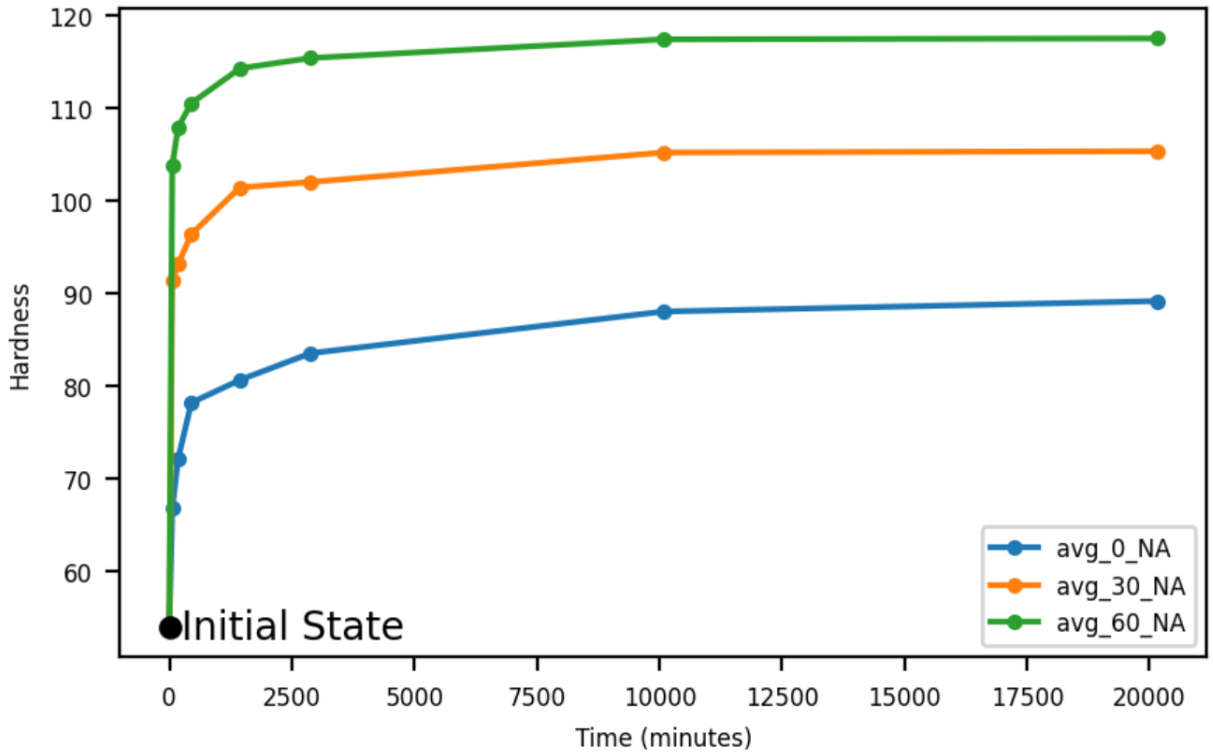

Figure 4.3: The diagram illustrates the development of hardness of samples 0-NA, 30-NA and 60-NA. The black point refers to the hardness value of sample IS.

According to the diagram above, it can be seen that the hardness increased at room temperature for all three samples over time. The effect of cold work is also obviously observable for samples 30-NA and 60-NA. The hardness increase was at its maximum after one hour (The first point after the black point) for all samples. The steep slope of the diagram for this interval (between 0-60 minutes) also proves this statement. However, after one hour, the slope of the diagram decreases over time

such that there are no significant changes in the hardness after one week (after 10080 minutes). The remarkable thing between diagrams is that the slope of the diagram for sample 0-NA is higher than the slope of other diagrams, except in the one-hour interval. In other words, the increase rate for sample 0-NA is higher than for other samples after one hour. This can also be verified by studying Table 4.3, as we see that for sample 0-NA, the difference between hardness values in different intervals is more than for samples 30-NA and 60-NA.

4.1.3 Natural vs. Artificial ageing

No new data will be presented in this subsection. Instead, the data presented in the previous subsections will be used. Figure 4.4 (see next page) indicates a diagram of the hardness development for samples 0-NA, 30-NA, and 60-NA, as well as the hardness value of samples 0-AA, 30-AA, and 60-AA as horizontal lines. The figure indicates that the hardness due to natural ageing did not reach the hardness due to artificial ageing (maximum values) for all samples after two weeks. The hardness due to natural ageing seems almost stable after one week (10080 minutes) and did not change too much after this time. Because of this reason, no new measurement was performed after two weeks.

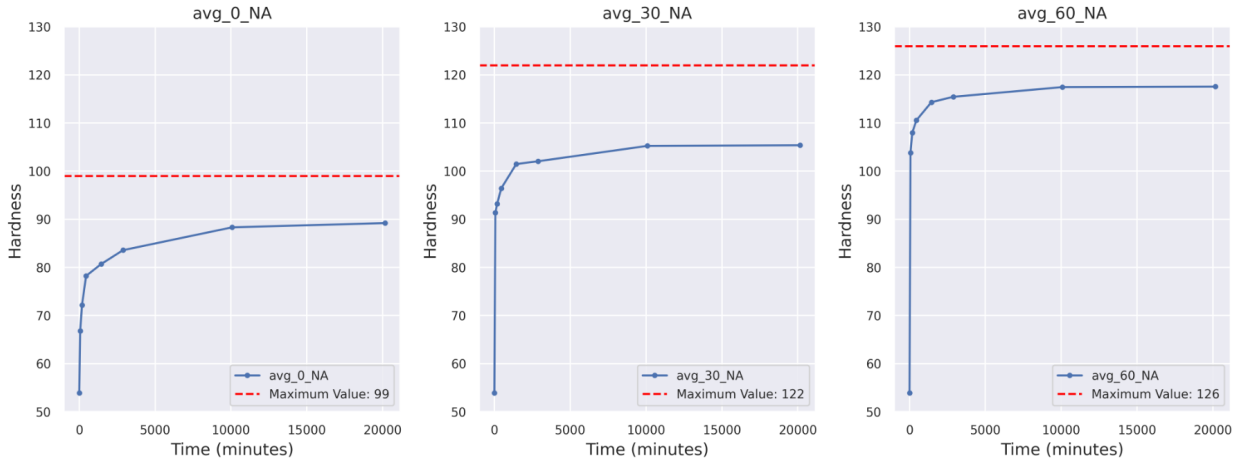

Figure 4.4: The diagram illustrates the hardness development of samples 0-NA, 30-NA and 60-NA. Horizontal lines indicate the hardness value due to Artificial ageing.

4.1.4 Effect of cold work on precipitation hardening

This section will compare the hardness values before and after precipitation hardening (natural and artificial ageing) to investigate the effect of cold work on precipitation hardening. No new data will be presented in this subsection. Instead, the data presented in the previous subsections will be used.

Table 4.4: The table compares hardness after artificial ageing with hardness after solution heat treatment for samples 0%, 30% and 60% deformed.

	one hour after SHT	after artificial ageing	difference
0 %	66.83	99.66	32.83
30 %	91.36	122.16	30.80
60 %	103.80	126.04	22.24

Table 4.5: The table compares hardness after two weeks natural ageing with hardness after solution heat treatment for samples 0%, 30% and 60% deformed.

	one hour after SHT	two weeks natural ageing	difference
0 %	66.83	89.20	22.37
30 %	91.36	105.38	14.02
60 %	103.80	117.56	13.76

Tables 4.4 and 4.5 compare the hardness of samples 0 %, 30 %, and 60 % deformed after precipitation hardening (after artificial ageing and after two weeks natural ageing) with the hardness after solution heat treatment for these samples. The hardness after solution heat treatment should be measured right after quenching and cold work. Still, since it took one hour to perform cold rolling and to prepare samples to test hardness, we relied on the hardness measured one hour after solution heat treatment. Both tables indicate that the difference between the hardness before and after precipitation hardening (artificial ageing and two weeks natural ageing) decreases for samples 30% and 60% compared to sample 0%. In other words, it seems that cold work prevents the hardness from increasing due to precipitation hardening for samples 30 % and 60 % as much as for sample 0 %.

In the discussion chapter, more details will be presented about the effect of cold work on precipitation hard-

ening based on the result of the hardness test.

4.2 Tensile test

This section is divided into three sub-sections to present and analyze the data efficiently.

4.2.1 Effect of precipitaion hardening

Only the data obtained for samples A-IS and A-0 (refer to Table 3.6 to review the definition of the abbreviations) can be used to evaluate the effect of precipitation hardening on the material. Table 4.6 compares the average

Table 4.6: Average yield strength, tensile strength and elongation for samples A-0 and A-IS. The average value is calculated as the mean of three specimens per sample.

Samples	A-IS	A-0
Avg. yield strength (MPa)	139.3	174.3
Avg. tensile strength (MPa)	145.3	273.3
Avg. strain (%)	12.22	22.49

yield strength, tensile strength and strain(elongation) for these two samples. Referring to Table 4.6, it is entirely observable that precipitation hardening affected and increased both the yield strength, tensile strength and elongation. However, this effect is much higher on the tensile strength and elongation than the yield strength. Upon examining Table 4.6, it becomes apparent that there was

an 88% increase in tensile strength, a 21.2% increase in yield strength, and an 84% increase in elongation.

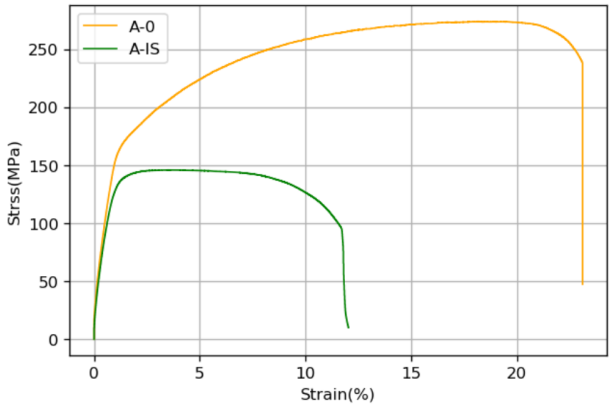

Figure 4.5: Stress-Strain diagram for samples A-0 and A-IS

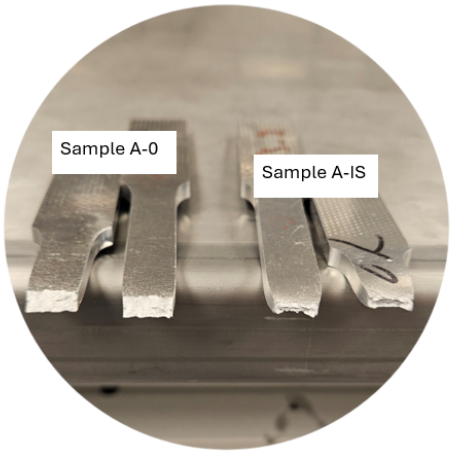

Figure 4.6: Fracture area of samples A-0 and A-IS.

In addition, Figure 4.5 above illustrates one of the stress-strain diagrams for these two samples in the ACR

direction (Refer to Appendix B to see all stress-strain diagrams). Figure 4.6 also shows an image of the fracture area of these samples as an example. Figure 4.6 does not present the fracture area of all samples, but since all other samples had a fracture area similar to that figure, they will not be given here. According to this figure, it indicates that sample A-IS experienced a higher reduction in area than sample A-0. In contrast, Figure 4.5 indicates that sample A-0 experienced higher elongation than sample A-IS. The amount of elongation and reduction in area can give us information about ductility, which will be discussed in the discussion chapter.

4.2.2 Cold work and precipitation hardening

Data for the samples A-0, A-30, and A-60 will be presented to study the effect of combining cold work and precipitation hardening. Table 4.7 presents these samples' average yield strength, tensile strength, and elongation. A bar plot, presented in Figure 4.7, is also provided to compare the average values visually.

Table 4.7: Average of yield strength, tensile strength and elongation for samples A-0, A-30 and A-60. The average value is calculated as the mean of three specimens per sample.

Samples	A-0	A-30	A-60
Avg. yield strength (MPa)	174.3	321.3	340.3
Avg. tensile strength (MPa)	273.3	339.3	365
Avg. elongation (%)	22.49	11.6	11.13

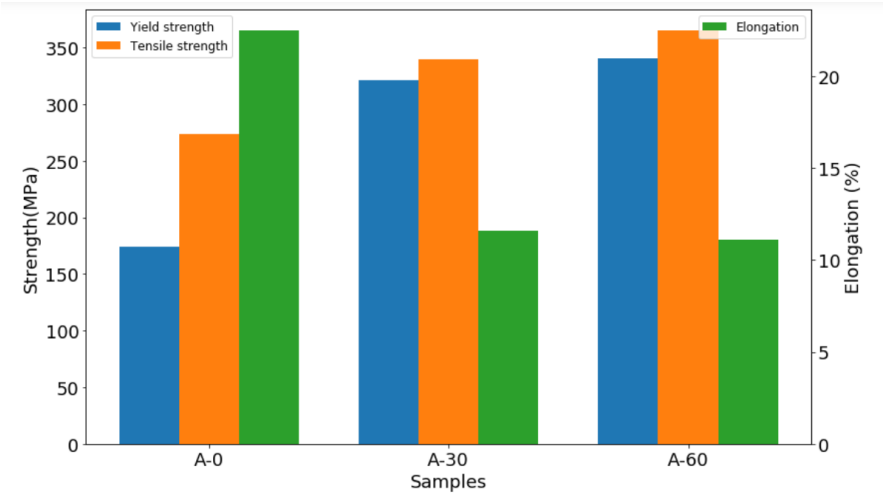

Figure 4.7: Three bar plots compare the average yield strength, tensile strength and elongation for samples A-0, A-30 and A-60.

Referring to Figure 4.7, the effect of the combination of cold work and precipitation hardening is obviously visible. Compared to sample A-0, which experienced only precipitation hardening, yield and tensile strength increased much more for samples A-30 and A-60 at the expense of reducing elongation. It is also notable that the yield strength of the material was improved significantly when cold work was combined with precipitation hardening. The bar plot for sample A-0 shows a significant difference between yield and tensile strength, while this difference becomes much smaller for samples A-30 and A-60. Comparing samples A-30 and A-60 also indicates that although sample A-60 is deformed twice as much as sample A-30, the difference between their yield strength, tensile strength and elongation is not extreme. Figure 4.8 (see next page) also presents the stress-strain diagrams of these samples. This figure represents only the diagram of one specimen for each sample, while three specimens were tested for each sample. To see all stress-strain diagrams for these samples, refer to Appendix B.

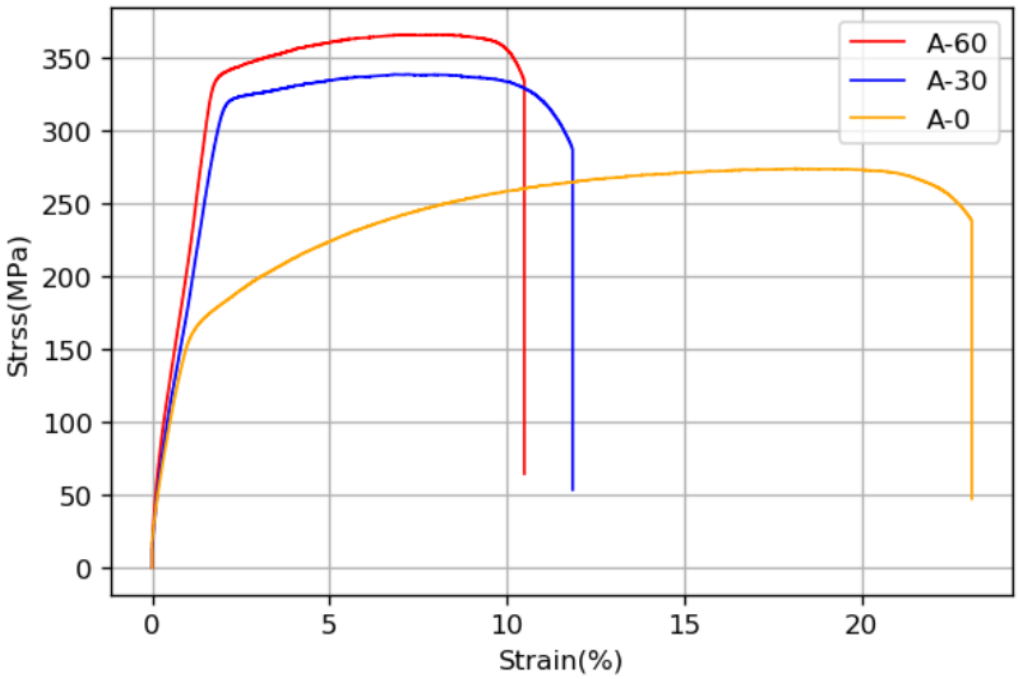

Figure 4.8: Stress-Strain diagram for samples A-0, A-30 and A-60

4.2.3 Anisotropy

This subsection will present the material's average yield strength, tensile strength and elongation in PCR and ACR directions. Tables 4.8 and 4.9 below indicate the average of yield and tensile strength, as well as elongation in PCR and ACR directions. In addition, Figure 4.9 presents three bar plots that compare the average values in these directions.

Table 4.8: Average yield strength, tensile strength and elongation for samples P-IS, P-0, P-30 and P-60. The average value is calculated as the mean of three specimens per sample.

Samples	P-IS	P-0	P-30	P-60
Avg. yield strength (MPa)	144	175.6	306	326
Avg. tensile strength (MPa)	149	273.3	330	346.3
Avg. elongation (%)	8.62	21.8	9.91	7.28

Table 4.9: Average yield strength, tensile strength and elongation for samples A-IS, A-0, A-30 and A-60. The average value is calculated as the mean of three specimens per sample.

Samples	A-IS	A-0	A-30	A-60
Avg. yield strength (MPa)	139.3	174.3	321.3	340.3
Avg. tensile strength (MPa)	145.3	273.3	339.3	365
Avg. elongation (%)	12.22	22.49	11.60	11.13

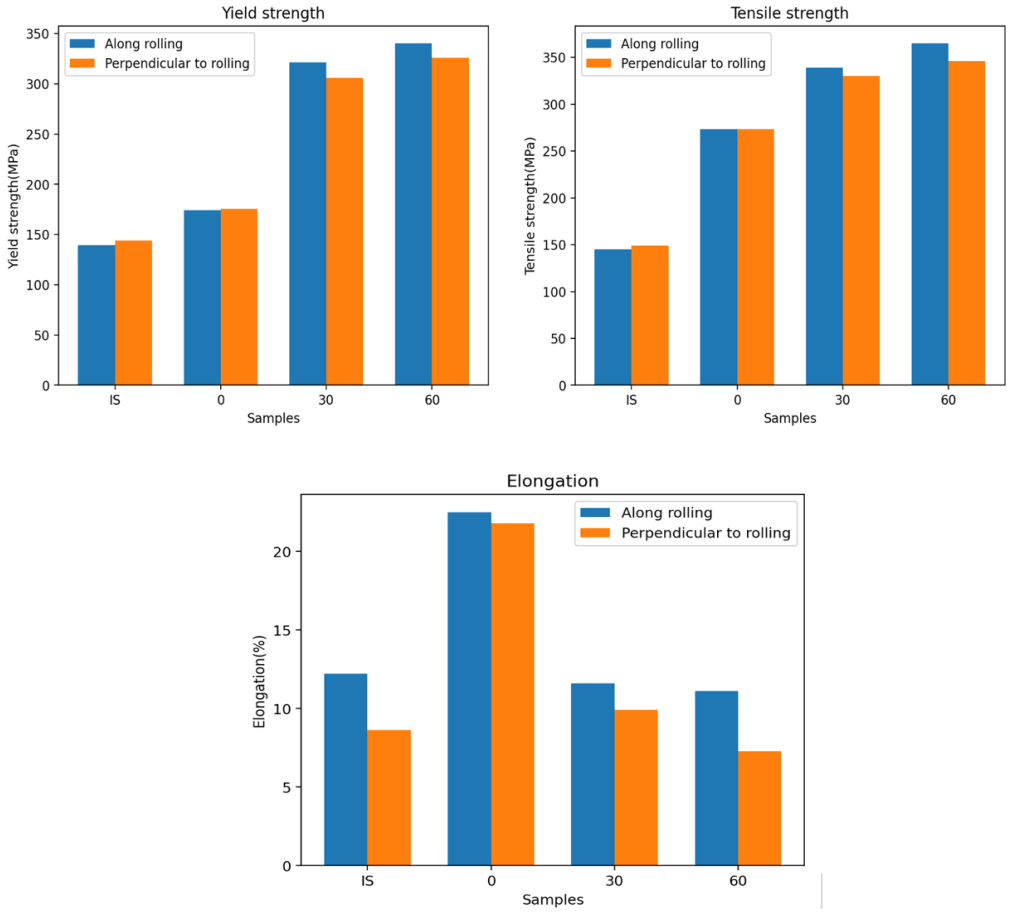

Figure 4.9: The bar plots compare the yield strength, tensile strength and elongation of samples IS, 0%, 30% and 60% in ACR and PCR directions.

Figure 4.9 shows samples with 30% and 60% deformation had greater yield and tensile strength in the ACR direction. In addition, since the elongation is higher in the ACR direction for these samples, the area under the stress-strain diagram should be greater for specimens tested in the ACR direction. Therefore, it can also be inferred that toughness is higher in the ACR direction than in the PCR direction. For the sample with 0% deformation, there is no difference in tensile strength between the ACR and PCR directions. However, the yield strength is higher by about 1.3 MPa in the PCR direction, which can be negligible. The difference between elongation for this sample in the ACR and PCR directions is also tiny. Regarding sample IS, there is little difference between yield and tensile strength in the ACR and PCR directions. The sample shows slightly higher strength (around 0-4 MPa) in the PCR direction. When it comes to elongation, there is an unusual result as the difference between elongation in the ACR and PCR direction is much higher for this sample compared to other samples.

4.3 Optical microscopy

This section presents all images of six samples with 0%, 30%, and 60% deformation from ACR and PCR planes after artificial ageing. Three different magnifications, namely 5X, 10X, and 20X, were used to study the microstructure of these samples. In addition, three different filters were used to observe grain and grain boundaries with different colours. It should be noted that using these filters without any electrolyte etching is useless, so electrolyte etching is required. The various colours of grains represent the crystallographic orientation of each grain. More details about crystallographic orientation will be discussed in the section regarding EBSD.

The first notable thing observed in all images in the figures 4.10, 4.12, 4.13 (see next pages) is that many black particles or pores are dispersed throughout the microstructure. By observing the images with higher magnification, for example, 20X, it seems that they are more similar to pores than particles, which may have been created during manufacturing. In the section regarding BSEs, we will also see that these pores, as well as some white particles, also dispersed for samples at the initial state and after solution heat treatment and, therefore, can not belong only to samples after artificial ageing.

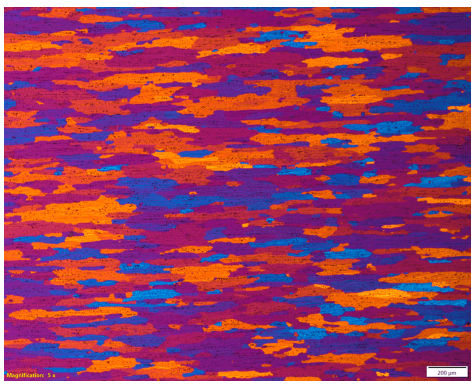

5X magnification, 200μm

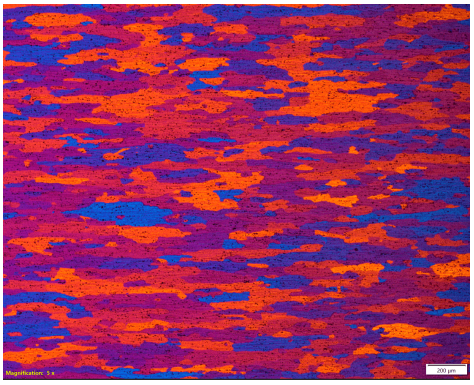

5X magnification, 200μm

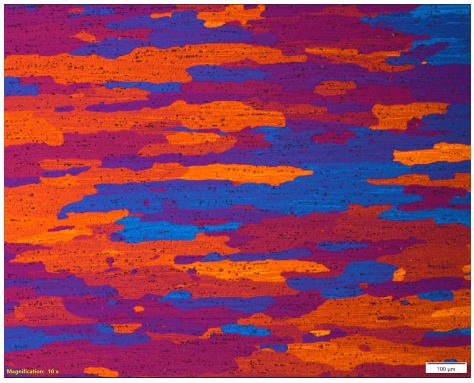

10X magnification, 100μm

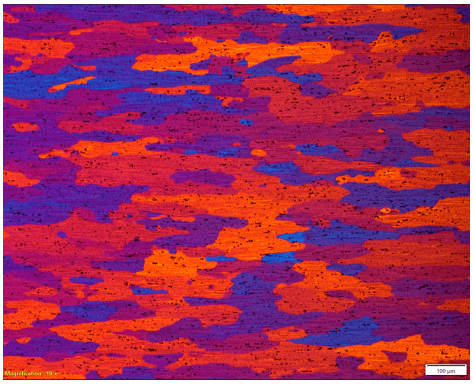

10X magnification, 100μm

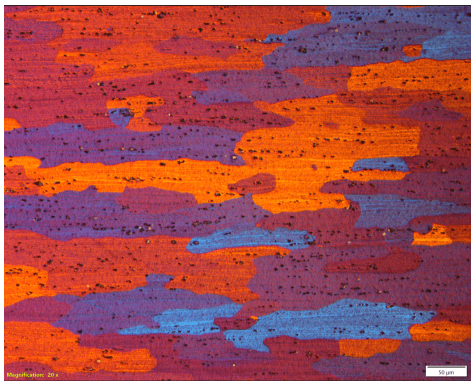

20X magnification, 50μm

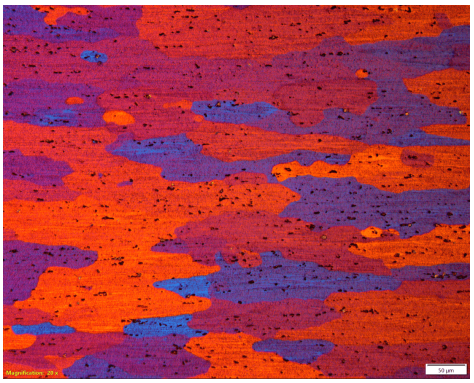

20X magnification, 50μm

Figure 4.10: Optical microscope images of sample 0 %. The column on the left represents the ACR plane, while the right represents the PCR plane.

Figure 4.10 presents the microstructure of the sample with 0 % deformation in planes ACR (left column) and PCR (right column). As mentioned earlier, the original plate had a rolling direction in advance. Therefore, it is not unexpected to see that grains in the ACR plane are somewhat elongated. Regarding the PCR plane, it seems that grains in this plane are also slightly elongated vertically (see Figure 4.11 below). Due to this, it is tough to distinguish the grain structures in these two planes.

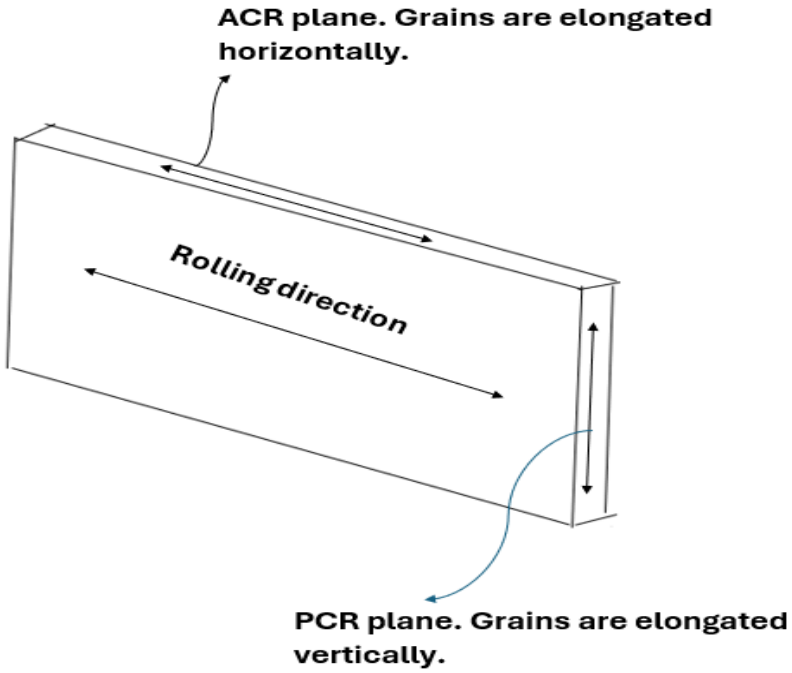

Figure 4.11: illustrates which direction grains in planes ACR and PCR are elongated.

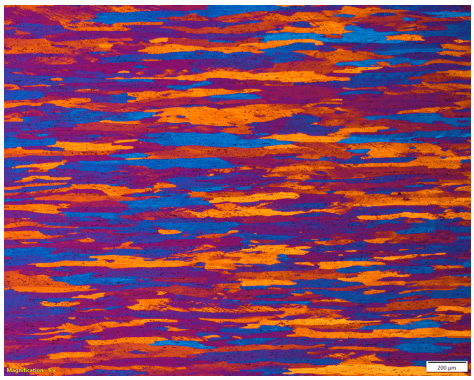

5X magnification, 200μm

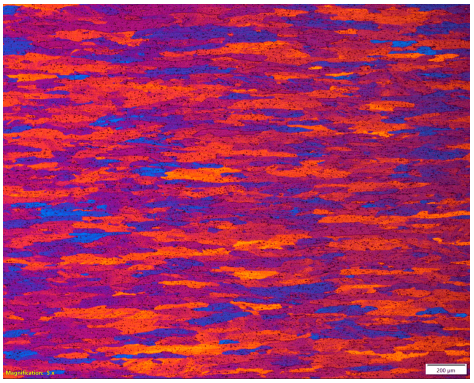

5X magnification, 200μm

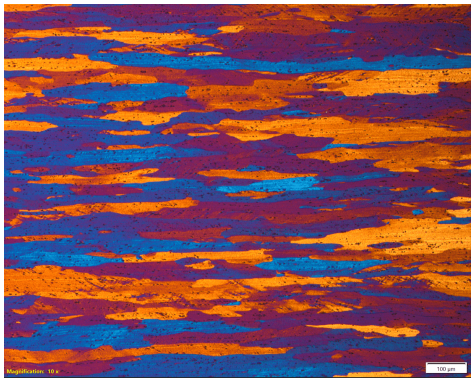

10X magnification, 100μm

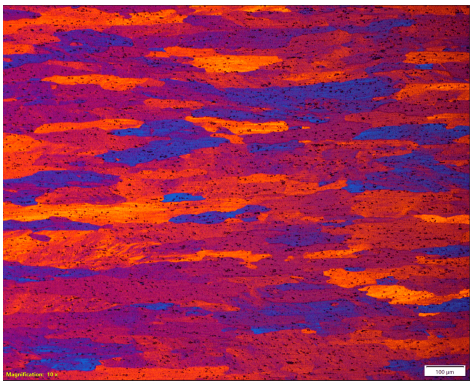

10X magnification, 100μm

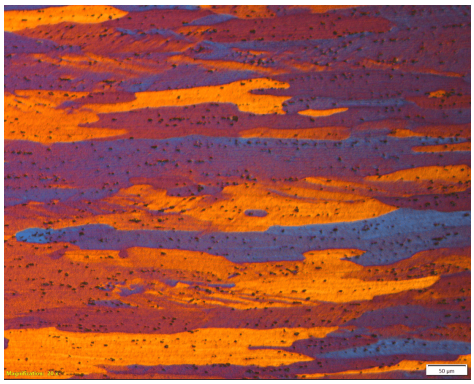

20X magnification, 50μm

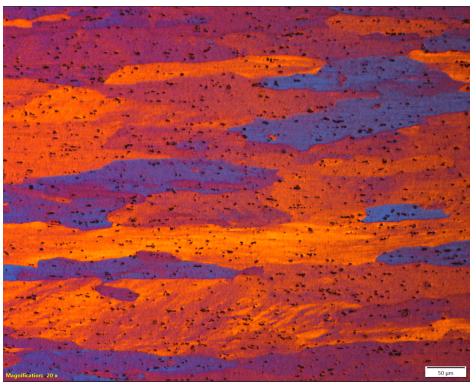

20X magnification, 50μm

Figure 4.12: Optical microscope images of sample 30 %. The column on the left represents the ACR plane, while the right represents the PCR plane.

Figure 4.12 presents the microstructure of the sample with 30 % deformation. Images above show that cold rolling has significantly affected the sample's microstructure as grains are more elongated and not as uniform and well-structured as sample 0%. In addition, it seems grains in the ACR plane are more elongated and compressed on each other than those in the PCR plane.

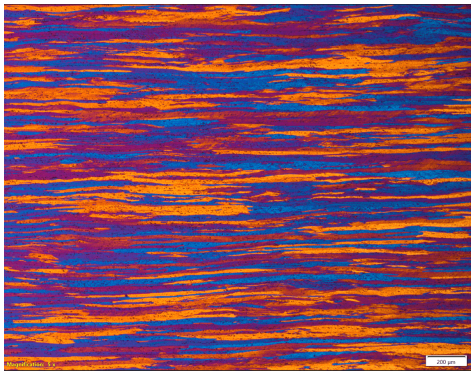

5X magnification, 200μm

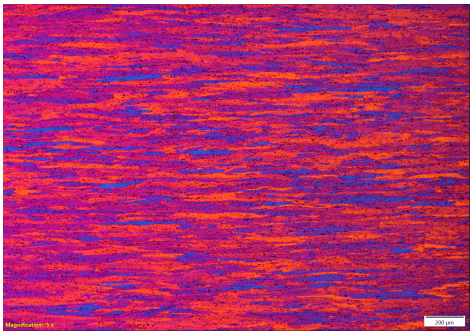

5X magnification, 200μm

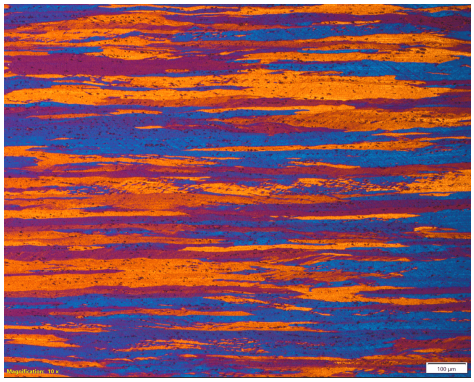

10X magnification, 100μm

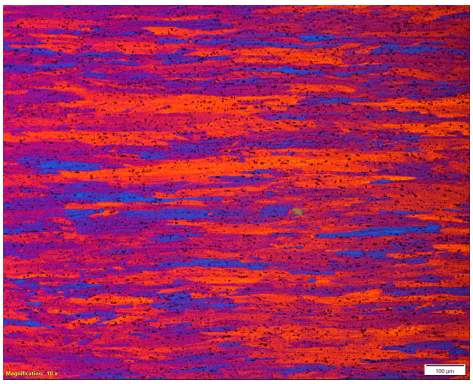

10X magnification, 100μm

20X magnification, 50μm

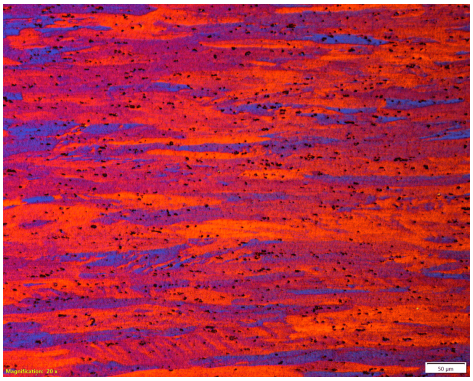

20X magnification, 50μm

Figure 4.13: Optical microscope images of sample 60 %. The column on the left represents the ACR plane, while the right represents the PCR plane.

Images in Figure 4.13 clearly show highly deformed microstructure due to cold rolling. The grains are more elongated compared to the sample with 30 % deformation. Like sample 30%, it is also observable that grains are much more elongated and compressed on each other in the ACR plane than those in the PCR plane. This difference in grain structure in these two planes can explain why the material showed higher hardness and strength in the ACR plane and ACR direction during mechanical tests. It will be discussed further in the discussion chapter.

4.4 Scanning Electron Microscopy

This section presents results from BSEs, EDS analysis and EBSD. SEM microscopy was conducted in several sessions. The first session was assigned to study the microstructure of samples 0 %, 30 % and 60 % after artificial ageing using Backscatter electrons (BSEs). As mentioned in subsection 3.6.4, many white particles were observed throughout the microstructure of all samples, and therefore, a new SEM session was done to find out how and when these white particles were created. In the new session, one sample from the original plate at its initial state (before any heat treatment and cold rolling) and one sample after solution heat treatment with 0 % deformation

were prepared to study the microstructure. This section starts by presenting the results of the Backscatter electorons.

4.4.1 Backscatter electrons

All images presented in this subsection were taken with the same aperture size of 60 μm and an accelerating voltage of 8kV. However, different degrees of magnification and varying working distance were used to highlight microstructure features. Figures 4.14 and 4.15 present the images of the sample IS (initial state) and sample after solution heat treatment using backscatter electrons.

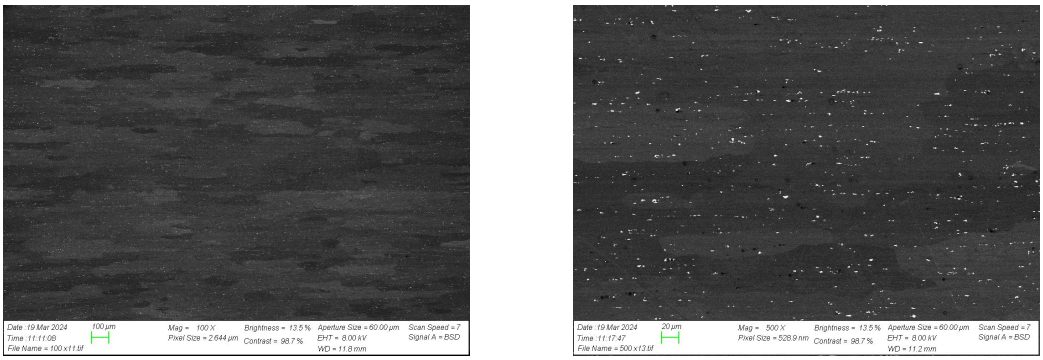

(a) 100X (b) 500X

Figure 4.14: Microstructure of sample IS with different magnifications (a): 100X and (b): 500X taken by Backscatter electrons.

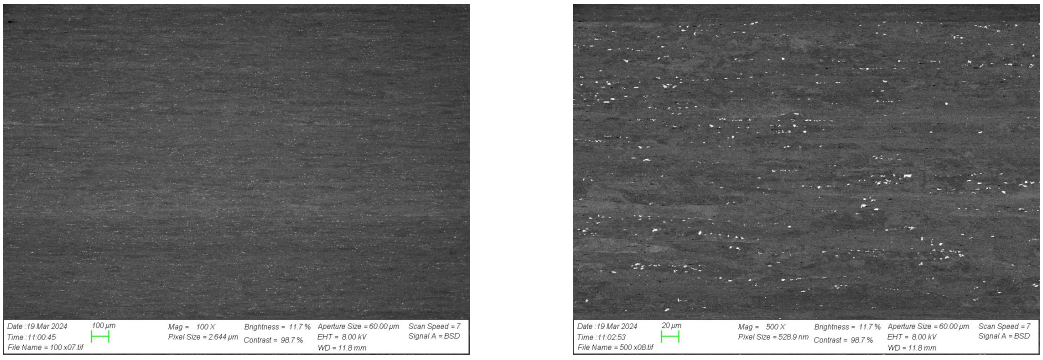

(a) 100X (b) 500X

Figure 4.15: Sample's microstructure after solution heat treatment with different magnifications (a):100X and (b):500X taken by Backscatter electrons.

Figures 4.14 and 4.15 clearly show that lots of white particles are dispersed throughout the microstructure of samples IS and the sample after solution heat treatment. In addition, by looking at the pictures with 500 magnification, we can see that many black particles or pores are also dispersed throughout the microstructure, which can be the same as those we observed earlier in the optical microscopy section. The existence of these particles for sample IS can tell us that these particles were introduced during the manufacturing of the material. It is also observable that the grains in both samples are slightly elongated horizontally, which is not unexpected since the original plate had a rolling direction in advance.

In addition, pictures with higher magnification (see Figure 4.16 on the next page), namely 5000 magnifica-

tion, were also taken of the samples to estimate the size of the particles. As seen in the figure below, the micron bar of the image is 2 μm. Comparing the micron bar with the particles, it can be concluded that some are roughly 2 μm, while many are less than 2 μm.

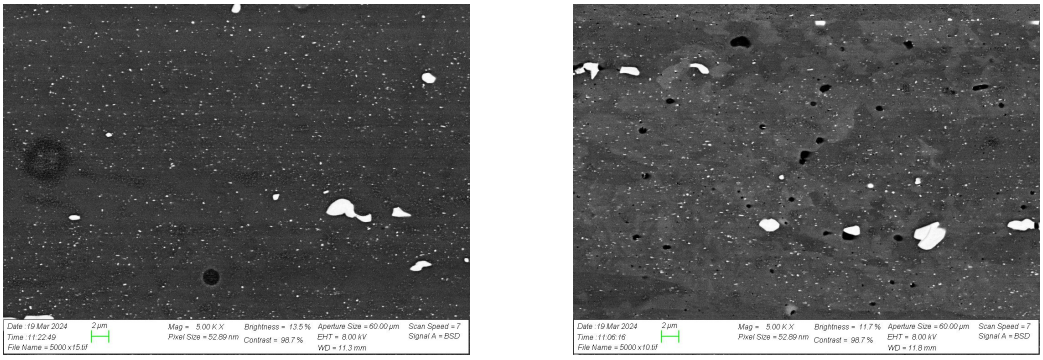

(a) Sample IS, 5000X (b) Sample after SHT, 5000X

Figure 4.16: Microstructure of (a): sample IS and (b): sample after SHT with 5000X magnification taken by Backscatter electrons. The length of the micron bar is 2 μm.

Figure 4.17 (see next page) presents the microstructure of samples 0 %, 30 %, and 60 % after artificial ageing.

The figure illustrates that the white particles are also dispersed throughout the entirety of all samples 0 %, 30 % and 60 %. However, black pores (particles) are relatively difficult to observe with 100X magnification, while some can be seen with 500X magnification. It should be noted that since the images were taken using varying working distances, brightness and contrast, it is possible to see some differences that should be ignored and not relied on.

Sample 0%, 100X

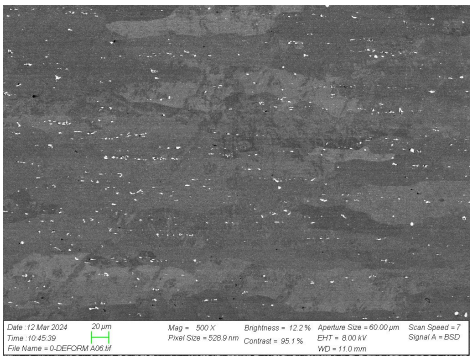

Sample 0%, 500X

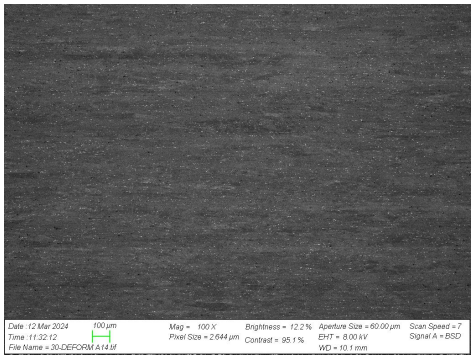

Sample 30%, 100X

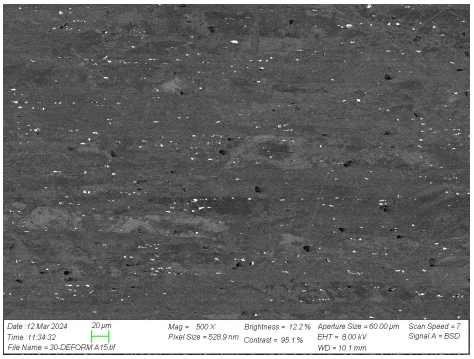

Sample 30%, 500X

Sample 60%, 100X

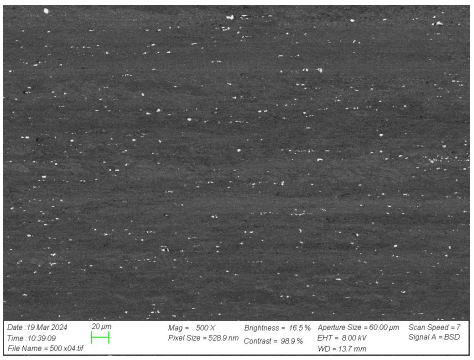

Sample 60%, 500X

Figure 4.17: Microstructure of samples 0 %, 30 % and 60 % with 100X and 500X magnifications taken by Backscatter electrons.

For example, black particles are more visible for samples 30 % compared to 0 % and 60 %. This does not mean that the amount or size of these particles is greater for sample 30 % as other images of 0 % and 60 % also show (not presented here) the same amount and size for these two samples. The images presented here are those with higher quality that primarily study the grain structure of the samples.

By comparing the images presented in Figure 4.17, it can be seen that cold rolling affected the grain structure as the grains are most elongated and thinner for the samples with 30 % and 60 % deformation.

4.4.2 EDS analysis

In this section, only the result of EDS analysis for sample 0 % will be presented as the other samples gave almost the same result. Figure 4.18 below indicates the selected spots and the area studied for EDS analysis.

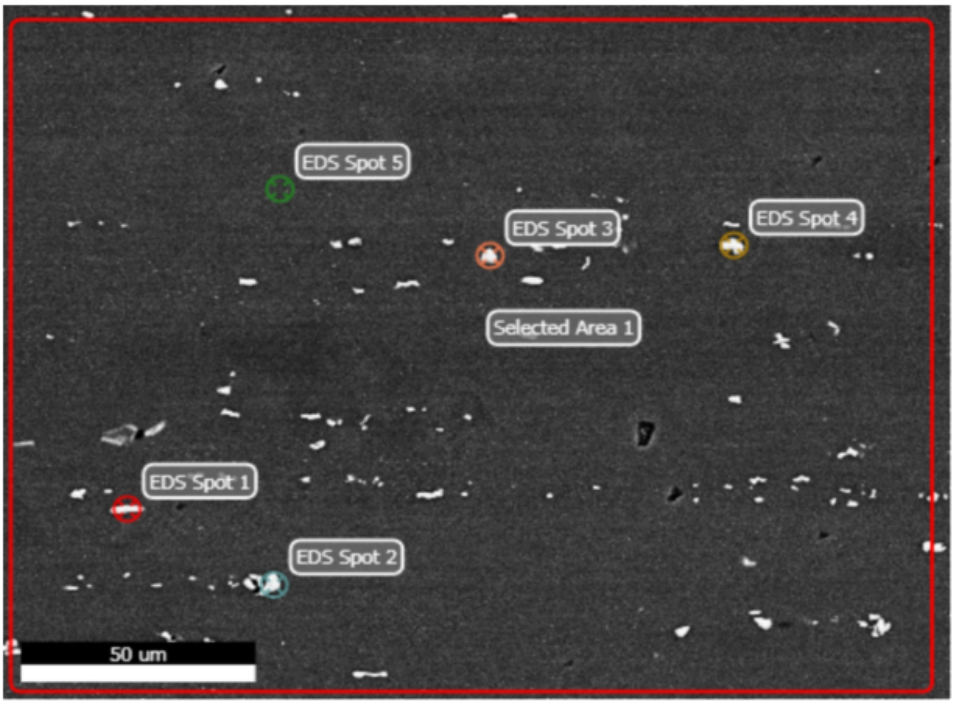

Figure 4.18: Selected spots and area in sample 0 % for EDS analysis

Among spots 1 to 4, only results of spot 4 will be presented. All these spots were selected to study the chemical composition of white particles, and therefore, their result was almost the same, and there was no significant difference between them. In addition to spot 4, the results of spot 5 and area 1 will also be presented to study the chemical composition of the matrix. Tables 4.10, 4.11 and 4.12 present elements, weight percentage, atomic percentage and error percentage of spots 4, 5 and area 1, respectively.

Table 4.10: Spot 4 (white particle)

Elements	Weight %	Atomic %	Error %
Al	42.76	59.95	3.75
Si	8.82	11.88	6.98
Cr	1.31	0.95	16.58
Mn	11.27	7.76	4.69
Fe	12.21	8.27	4.89

Table 4.11: Spot 5

Elements	Weight %	Atomic %	Error %
Mg	1.07	1.51	5.26
Al	66.46	84.54	2.23

Table 4.12: Area 1

Elements	Weight %	Atomic %	Error %
Mg	0.95	1.32	5.63
Al	68.21	85.60	2.18

By comparing the tables above to the known chemical composition (see Table 3.1 in the Experimental chapter), most of the elements were identified by EDS analysis, and only two elements, namely Cu and Zn, were not found either in the white particles or the matrix. In addition, the weight and atomic percentages presented in the tables above can not be reliable because of analyzing a small area.

4.4.3 EBSD

As mentioned in section 3.6.4, only plane ACR were studied for samples 0 %, 30 % and 60 %. This section will be divided into three subsections, each presenting the EBSD images, Pole figures and Grain size determination.

EBSD images

Figure 4.19 indicates the EBSD image and inverse pole figure for sample 0 %.

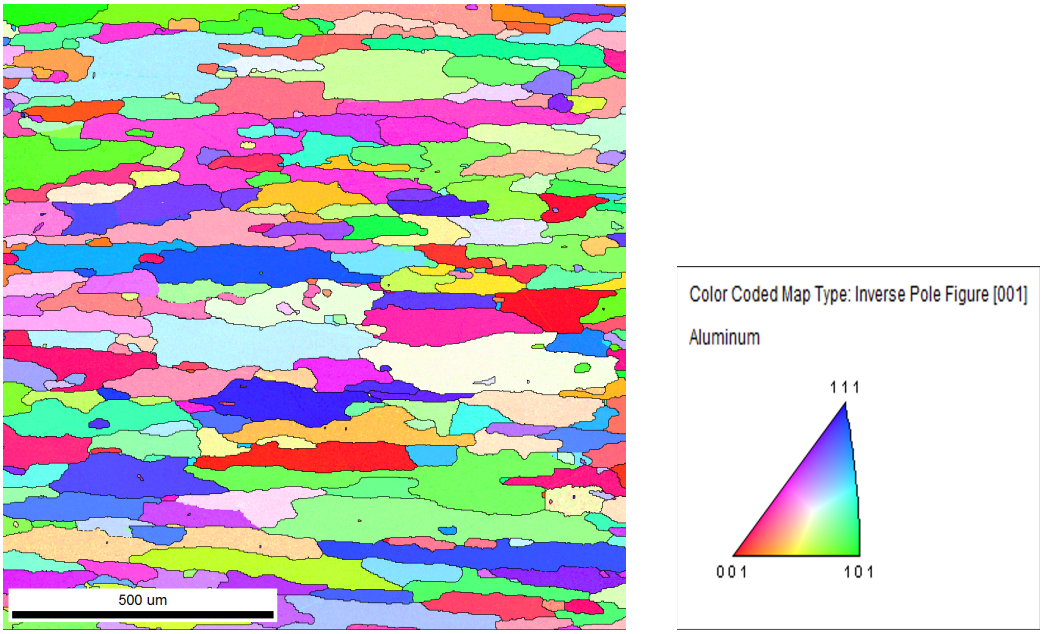

(a) (b)

Figure 4.19: EBSD image and inverse pole figure for sample 0 %. The length of the micron bar is 500 μm

As expected, Figure 4.19 above indicates that the grains are horizontally elongated for sample 0 % since the material experienced hot work during fabrication and, therefore, had a rolling direction in advance. The EBSD image shows a grain structure similar to that taken by optical microscopy. However, we can now safely discuss the crystallographic orientation using the EBSD image and

inverse pole. The crystallographic orientation for sample 0 % seems to be varied between ⟨111⟩, ⟨001⟩ and ⟨101⟩ direction, and it is tough to determine any preferred orientation for the grains.

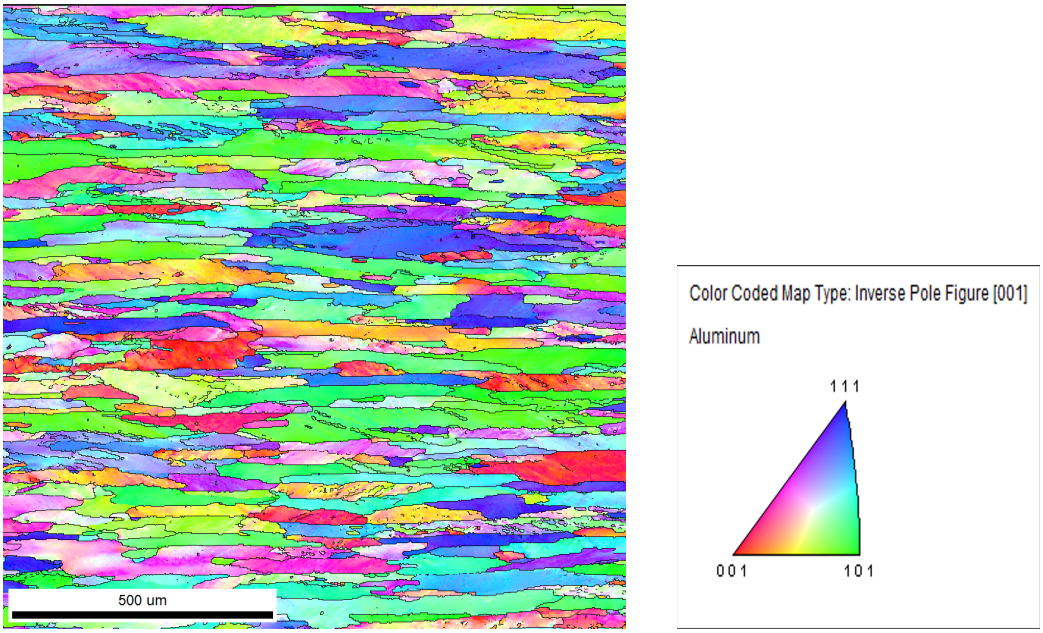

(a) (b)

Figure 4.20: EBSD image and inverse pole figure for sample 30 %. The length of the micron bar is 500 μm

Figure 4.20 above illustrates the EBSD image of sample 30 %. The image indicates that the cold rolling has affected the grain structure; therefore, they became more elongated compared to sample 0 %. In addition, it seems that some small subgrains started to be formed in the larger grains due to cold rolling. Identifying any preferred orientation for the grains in this sample remains

difficult, similar to sample 0 %.

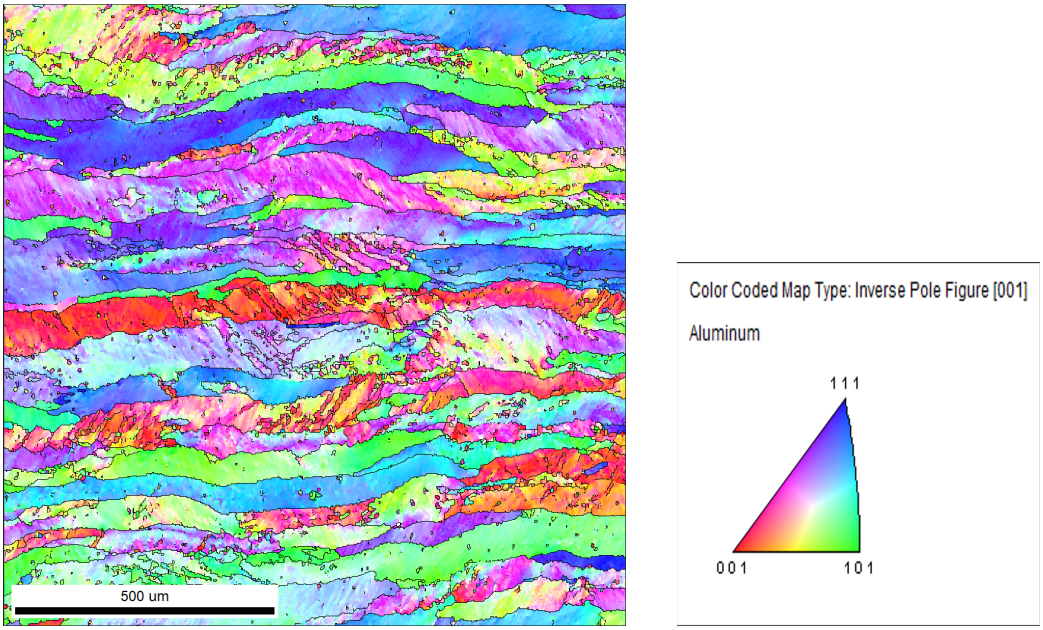

(a) (b)

Figure 4.21: EBSD image and inverse pole figure for sample 60 %. The length of the micron bar is 500 μm

Figure 4.21 shows that the cold rolling has significantly affected the grain structure of sample 60 %. Compared to sample 30 %, grains have been more elongated, and more subgrains have been formed in the larger grains. In addition, we can see that although the crystallographic orientation still varies between $\langle 111 \rangle$, $\langle 001 \rangle$ and $\langle 101 \rangle$ direction, it seems that most of the grains favour the $\langle 111 \rangle$ direction.

Pole figures

Images of pole figures will be presented here. These pole figures will be used to discuss the possible existence of texture due to cold work.

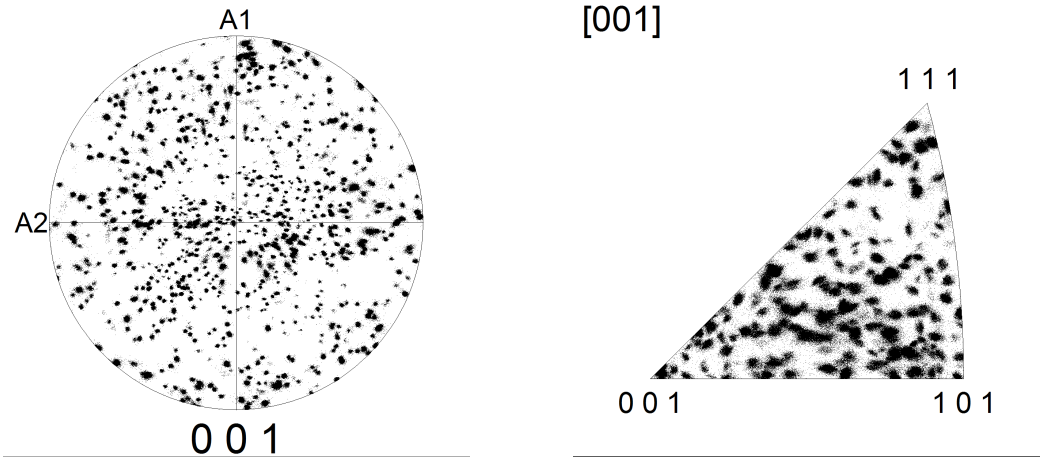

(a) (b)

Figure 4.22: Pole figure for sample 0 %

Figure 4.22 illustrates the pole figure of sample 0 %. It can be seen that dark areas are dispersed randomly, and therefore, there is no sign of the formation of any pattern in the pole figure of sample 0 %. In other words, no texture or preferred grain orientation could be seen in this sample.

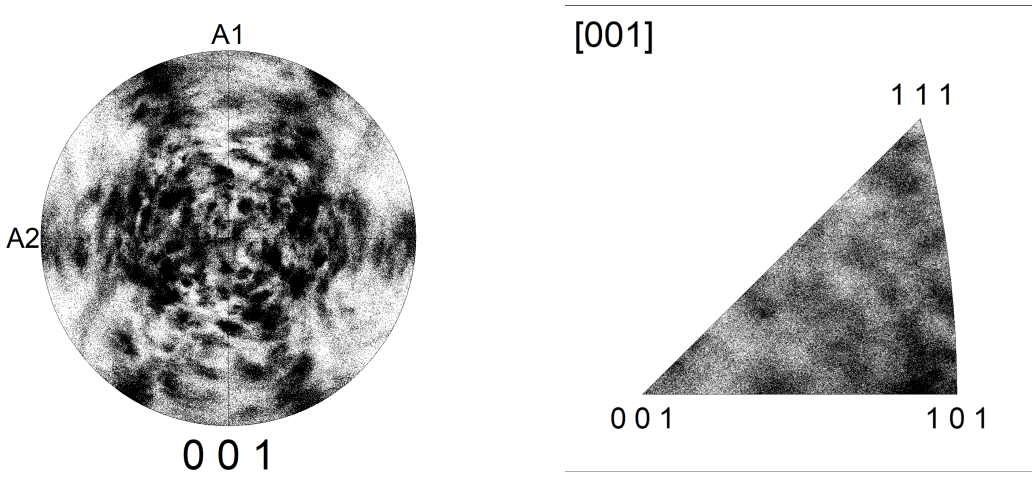

(a) (b)

Figure 4.23: Pole figure for sample 30 %

Figure 4.23 represents the pole figure of sample 30 %. Compared to sample 0 %, the dispersion of dark areas is completely reduced. The accumulation and high volume of these dark areas represent the specific orientation of the grains. It is clear that the cold work was somewhat effective, and a particular pattern started to form in the pole figure. Figure 4.23b also shows that the dark areas are relatively dispersed, although the density of these dark areas seems slightly higher near the $\langle 101 \rangle$ direction.

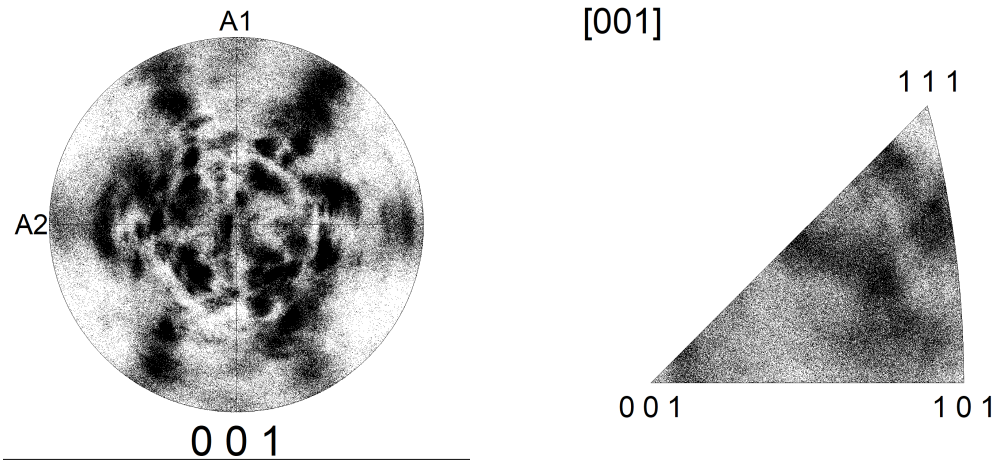

(a) (b)

Figure 4.24: Pole figure for sample 60 %

Figure 4.24 represents the pole figure of sample 60 %. Compared to sample 30 %, the dispersion of dark areas is reduced. It can be said that a specific pattern is formed for sample 60 %. Figure 4.24b also shows that the dark areas have moved towards the $\langle 111 \rangle$ direction. Overall, it can be inferred that cold work clearly affected the material's microstructure, and texture has, to a high degree, formed.

Grain size determination

This subsection presents the effect of cold work and heat treatments on the average grain diameter of the samples 0 %, 30 % and 60 % using the linear intercept method. This method was explained earlier in section 3.6.4.

Table 4.13 presents the average intercept length for these samples. See Appendix C for the bar plot and numerical data for all three samples.

Table 4.13: Average intercept length for samples 0 %, 30 % and 60 %

Samples	0 %	30 %	60 %
Average intercept length	55.539 μm	39.691 μm	17.577 μm

Referring to Table 4.13, sample 0 % has the highest value of the grain size, which was not unexpected as this sample did not experience any cold deformation. As we observed in the EBSD images, high deformation due to cold work caused forming thinner grains and small subgrains in the material's microstructure. Therefore, sample 60 % has the lowest value of the grain size.

5 Discussion

5.1 Hardness

The following subsections will be discussed according to the results presented in section 4.1.

5.1.1 Cold work and precipitation hardening

As expected, the combination of cold work and precipitation hardening had a remarkable impact on the hardness of the material. Without any cold deformation, the hardness increased in natural ageing to 89.20 HV10 (after two weeks) and in artificial ageing to 99.32 HV10. This proves that the precipitation hardening was successful to a high degree.

When cold work was combined with precipitation hardening (natural and artificial ageing) in samples with 30% and 60% deformation, the hardness increased much more compared to the sample 0%, which was treated by only precipitation hardening. This result indicates that the combination of cold work and precipitation hardening was also highly successful.

Furthermore, it can also be concluded that as the degree of deformation increases, the material's strength increases since the sample with 60% deformation had a higher hardness value than 30%.

5.1.2 Effect of cold work on precipitation hardening

According to the results obtained in section 4.1, it can be seen that cold working impacts the precipitation hardening process by slowing down the rate of hardness increase during precipitation hardening over time. This effect can be seen both in the natural ageing process and in the artificial ageing process.

Regarding the natural ageing process, we can refer to Figure 4.3. By comparing the diagrams after one-hour intervals for three samples, 0-NA, 30-NA and 60-NA, it can be seen that the slope of the diagram (after 1-hour interval and later) for the 0-NA sample is steeper than the 30-NA and 60-NA sample. In addition, by referring to Table 4.3, it is clear that the average hardness for the 0-NA sample in different time intervals has greater changes than the 30-NA and 60-NA samples. Table 4.5 also, by comparing the hardness values between two points (after two weeks natural ageing and after solution heat treatment), indicated that the hardness increase for sample 0 % was the highest (22.37 HV10), while it decreased for samples 30 % and 60 % to 14.02 HV10 and 13.76 HV10, respectively.

We can refer to Figure 4.1 and Table 4.4 regarding the artificial ageing process. Figure 4.1 illustrated the bar plot of hardness value for samples IS, 0-AA, 30-AA and

60-AA. The notable point was that although sample 60-AA has been deformed as double that of sample 30-AA, the difference between their hardness is only 4 HV10. It seems that sample 60 % did not experience too much hardness increase during artificial ageing compared to sample 30 %. This can imply that as the degree of deformation due to cold work increases, the rate of growth in hardness due to artificial ageing decreases (all samples experienced 8 hours of artificial ageing). Table 4.4 also verifies this statement by comparing the hardness values for samples 0%, 30% and 60% between two points (after solution heat treatment and artificial ageing). As the table indicated, the difference between hardness values for sample 0% was highest (32.83 HV10), and as the degree of deformation increased to 30% and 60%, the difference decreased to 30 HV10 and 22 HV10, respectively.

Microscopic investigation of the material's microstructure can be instrumental in observing and studying how cold working affects precipitation hardening from a microscopic view. As mentioned in the theory chapter, section 2.6, cold work induces dislocations and vacancies, affecting precipitation kinetics during ageing. However, the relation to how cold work affects GP zones or precipitate particles and how these particles dispersed throughout the microstructure of the alloy 6082 requires microscopic

technologies such as TEM, which are not covered here.

5.1.3 Anisotorpy

Figure 4.2 (see result chapter, section 4.1.1) can be utilized to study the existence of anisotropy resulting from cold work. The bar plot in this figure compares the hardness value in planes PCR and ACR. All samples had higher hardness on the ACR plane, indicating that anisotropy exists to some degree in all samples. However, it is difficult to conclude that anisotropy exists clearly for samples IS and 0-AA since the standard deviation calculated for these samples can show that the hardness in both ACR and PCR planes may be equal. In return, it can be concluded that due to cold rolling, anisotropy is observed for samples 30-AA and 60-AA since the difference between hardness is high enough for these samples. This difference suggests that cold rolling had a higher effect on the material's grain structure in the ACR plane than in the PCR plane. In other words, the increase in dislocation density resulting from cold rolling is higher in the ACR plane than in the PCR plane. Therefore, the ACR plane indicates higher strength due to more impeding the dislocation movements.

5.2 Tensile test

The following subsections will be discussed according to the results presented in section 4.2.

5.2.1 Effect of precipitation hardening

As expected, precipitation hardening affected the material's mechanical properties, such as yield strength, tensile strength, ductility, and toughness. Since the increase in yield strength is much less than the increase in tensile strength, it can be inferred that precipitation hardening affects the tensile strength of the material much more than yield strength. However, as time and temperature play an essential role in the precipitation process, modifying time and temperature can reject this inference.

According to the results obtained, it can be seen that precipitation hardening significantly increased the toughness of the material. The area under the stress-strain curve for sample A-0 is much greater than that for sample A-IS, as shown in Figure 4.6. When it comes to ductility, although sample A-0 was elongated more than sample A-IS, it can not be concluded that sample A-0 is more ductile. The image presented in Figure 4.6 indicated that sample A-IS had a higher reduction in area, implying that it is more ductile than sample A-0. However, to

determine the ductility of these samples with higher accuracy, a fractography analysis using SEM microscopy is required. This thesis does not cover this analysis and may be conducted as further work.

5.2.2 Cold work and precipitation hardening

The data presented in subsection 4.2.2 clearly showed the positive effect of the combination of cold work and precipitation hardening on the material's mechanical properties. This combination increased both yield and tensile strength to a high degree. However, this positive effect was the expense of reducing the material's ductility as elongation reduced significantly for samples A-30 and A-60. The interesting point is that cold work improved the yield strength of the material, which had not been increased too much due to only precipitation hardening. This phenomenon was expected as Figure 2.4 in the Theory chapter, section 2.5.3 indicated how cold work can enhance the yield strength point after deformation.

Another notable point is that there is not too much difference between the values of mechanical properties for sample A-30 and A-60, while sample A-60 was deformed twice as much as sample A-30. This phenomenon was also observed when we discussed hardness. Again, the results of the tensile test show that cold work affected

the precipitation formation and, as a result, the rate of change in mechanical properties (increase in strength and decrease in elongation) due to precipitation hardening decreased as the amount of deformation increased.

5.2.3 Anisotropy

Based on Figure 4.9 (see result chapter, section 4.2.3), it can be safely concluded that the anisotropy resulting from cold work is observed in samples 30% and 60%. Yield strength, tensile strength and elongation are different to a high degree for these samples in the PCR and ACR directions. The difference is also higher for sample 60 % as it is deformed twice the sample 30 %. The results indicated that yield strength, tensile strength and toughness were higher in the ACR direction than in the PCR direction. Regarding ductility for these samples, a fractography analysis is required to study the fracture area to determine the amount of ductility in the ACR and PCR directions. However, The results for these samples (30 % and 60 %) verified our previous findings (refer to the hardness section, subsection 5.1.3) that cold rolling had a higher impact on the grain's structure in the ACR plane, resulting in a greater increase in the density of dislocations in this plane than in the PCR plane.

For sample 0 %, the difference between its mechanical

properties is very minimal, and it can not be inferred that the anisotropy exists for this sample. The same conclusion could be inferred for sample IS regarding yield and tensile strength, as there is no significant difference between them in the ACR and PCR directions. However, considering the elongation of this sample in the ACR and PCR directions, it can reject our conclusion as there is a high difference between elongation in these directions. Determining the existence of anisotropy for this sample requires more information regarding previous operations the material underwent during manufacturing.

5.3 Optical microscopy

Optical microscopy was conducted on ACR and PCR planes of samples with 0 %, 30 % and 60 % deformation. All of these samples experienced artificial ageing. Studying the planes ACR and PCR of sample 0 % showed no specific difference between the microstructure in these two planes. Grains in both planes were slightly elongated, which can result from previous hot work the material experienced during manufacturing. This similarity between grains in these two planes was expected since the result of the tensile test and hardness also indicated that the anisotropy in this sample was not observed clearly. Regarding samples 30 % and 60 %, a clear difference between

the grain structures of these two planes was observed as expected since we observed anisotropy for these samples during mechanical tests. The results of the mechanical tests showed that samples 30 % and 60 % showed higher hardness and strength in the ACR plane and ACR direction, respectively. These results can be justified by studying the grain structures of these samples. According to Figures 4.12 and 4.13, grains in the ACR plane are more deformed (more elongated and compressed on each other) for samples 30 % and 60 %. This higher deformation in the ACR plane can signify greater dislocation density in this plane. Referring to the theory chapter, section 2.5.3, increasing dislocation density leads to more hindrance to dislocation motion. As a result, the samples would show higher strength during mechanical tests.

5.4 SEM

SEM was conducted only on the ACR plane of samples 0 %, 30 % and 60 %. All of these samples experienced artificial ageing. Images from BSEs showed the effect of cold work on the material's microstructure as we observed that grains of samples with 30 % and 60 % were elongated more in the cold rolling direction. Regarding EDS analysis, the results were mainly satisfactory. The elements shown by EDS analysis were broadly consistent with the

known chemical composition in Table 3.1, presented in the experimental chapter. The difference in the amount of these elements with the values given in Table 3.1 can be because a small area of the material's microstructure was studied. The results from EBSD gave notable information about grain orientation, texture, and grain size. The results were consistent with our expectations. As expected, grains in sample 0 % had random orientation varying between $\langle 111 \rangle$, $\langle 001 \rangle$ and $\langle 101 \rangle$ directions. This random orientation significantly reduced for sample 60 % as we observed that grains in this sample favoured the $\langle 111 \rangle$ direction. The Pole figure of sample 60 % also indicated a clearer pattern of dark areas compared to samples 30 % and 0 %. This shows the signs of texture formation due to cold work for this sample. As expected, the linear intercept method also determined that grain size was reduced as cold work increased from 0 to 30 and 60 per cent.

6 Errors and limitaions

This section presents the potential errors and limitations that may have affected the accuracy of the results presented in this thesis.

1. Manual measurement: All of the measurements in this thesis were done manually with a ruler and digital calliper. Potential human errors can be considered for all of these measurements.

2. Inaccurate amount of deformation: The amount of thickness reduction by cold rolling could not be reached precisely due to a tiny misalignment of the machine's rollers and manual measurement of the amount of reduction using a hand clock installed on the machine.

3. Challenges during the tensile test: The clamps of the tensile test machine could not hold the head of some specimens stably. In addition, installing an external extensometer on the sample stably and without sliding was not entirely possible for some tensile test specimens. Due to these challenges, stress-strain diagrams of some specimens contained slight noise, and because of that, all stress-strain diagrams were redrawn using raw data generated by the tensile test machine.

4. Small number of indentations in hardness test: Only five indentations were conducted for all hard-

ness tests in this thesis. The higher number of indentations could give more accurate results.

5. Imaging of small areas in SEM and Optical microscopy: Small areas were selected to produce images of the material's microstructure using SEM and Optical microscopy. In addition, due to lack of time, only some specific planes were studied under microscopy. Studying larger areas and different planes of the samples might give us more information about the material's microstructure.

6. Adjusting the time and temperature of the ageing process: Adjusting the required time and temperature defined in the ageing process may not be reached accurately due to human errors or possibly inaccuracy in the furnace's thermostat.

7 Conclusion

Based on the investigation performed in this thesis, the combination of cold work and precipitation hardening significantly enhanced the strength of aluminium alloy 6082. Additionally, it revealed that cold work diminishes the effect of precipitation hardening on the material's strength.

Mechanical tests, including hardness and tensile tests, showed that as the degree of deformation increases, precipitation hardening's effect on mechanical properties seems to decline for the aluminium alloy 6082. However, both tests illustrated that combining cold work and precipitation hardening impacts the alloy's strength more than only performing one.

Optical microscopy and Scanning Electron microscopy revealed the effect of cold work on grain structure and orientation, with a notable reduction in grain size with increased deformation.

As further work, the time and temperature of the precipitation hardening process can be modified to observe the improvement or unimprovement of mechanical properties due to this modification. In addition, a TEM investigation can be employed to see the formation of precipitate particles in the microstructure of the samples with different degrees of deformation due to cold rolling. This

investigation may give us a more precise conclusion of the effect of cold work on precipitation hardening. Fractography analysis can be employed to study the fracture area of the tensile test specimens to investigate the amount of ductility for these specimens tested in ACR (along cold rolling) and PCR (perpendicular to cold rolling) directions. Finally, a further investigation can be performed to compare natural ageing against artificial ageing in more detail.

References

[1] W. D. Callister and D. G. Rethwisch, *'Intorduction,' in Materials science and engineering*, 9th ed. USA: Wiley, 2013, ch. 1, p. 6.

[2] W. D. Callister and D. G. Rethwisch, *'Applications and Processing of Metal Alloys,' in Materials science and engineering*, 9th ed. USA: Wiley, 2013, ch. 11, p. 422.

[3] W. D. Callister and D. G. Rethwisch, *'Applications and Processing of Metal Alloys,' in Materials science and engineering*, 9th ed. USA: Wiley, 2013, ch. 11, p. 425.

[4] J. R. Davis, *'Wrought Products,' in Aluminum and Aluminum alloys*, 1st ed. USA: ASM International, 1994, ch. 2, p. 59.

[5] AZO. "Aluminium alloys - aluminium 6082 properties, fabrication and applications." Accessed: January 22, 2024. (Apr 21 2005), [Online]. Available: https://www.azom.com/article.aspx?ArticleID=2813.

[6] jrfurnace. "What is solution heat treatment and why is it important?" Accessed: February 24, 2024. (), [Online]. Available: https://www.jrfurnace.net/what-is-solution-heat-treatment-and-why-is-it-important/.

[7] W. D. Callister and D. G. Rethwisch, *' Heat Treatments,' in Materials science and engineering*, 9th ed. USA: Wiley, 2013, ch. 11, pp. 453–457.

[8] testbook. "Defects in crystal structure: Types of defects, semiconductor, electrical and magnetic properties." Accessed: February 3, 2024. (May 2023), [Online]. Available: https://testbook.com/chemistry/defects-in-crystal-structure#:~:text=Defects%20in%20Crystal%20Structure%20are,or%20neutrons)%20striking%20the%20solid..

[9] W. D. Callister and D. G. Rethwisch, *'Point Defects,' in Materials science and engineering*, 9th ed. USA: Wiley, 2013, ch. 4, pp. 106–107.

[10] J. Kośmider, *Defect of crystal structure*, https://upload.wikimedia.org/wikipedia/commons/b/b5/Cryst_struct_deficit.svg, [accessed February 1, 2024], 2011. [Online]. Available: https://commons.wikimedia.org/wiki/File:Cryst_struct_deficit.svg.

[11] W. D. Callister and D. G. Rethwisch, *'DISLOCATIONS—LINEAR DEFECTS ,' in Materials science and engineering*, 9th ed. USA: Wiley, 2013, ch. 4, p. 115.

[12] W. D. Callister and D. G. Rethwisch, *'Mechanisms of Strengthening in Metals,' in Materials science and engineering*, 9th ed. USA: Wiley, 2013, ch. 7, p. 229.

[13] W. D. Callister and D. G. Rethwisch, *'SLIP SYSTEMS ,' in Materials science and engineering*, 9th ed. USA: Wiley, 2013, ch. 7, p. 221.

[14] W. D. Callister and D. G. Rethwisch, *'POLYCRYSTALLINE MATERIALS ,' in Materials science and engineering*, 9th ed. USA: Wiley, 2013, ch. 3, p. 84.

[15] T.-T. Fang, *Elements of structures and defects of crystalline materials*, eng. Amsterdam, Netherlands: Elsevier, 2018, pp. 174–176, ISBN: 0-12-814269-3.

[16] W. D. Callister and D. G. Rethwisch, *'Solid Solution Strengthening,' in Materials science and engineering*, 9th ed. USA: Wiley, 2013, ch. 7, p. 231.

[17] Zerodamage, *Substitutional solute*, https://upload.wikimedia.org/wikipedia/commons/6/63/Substitutional_solute.svg, [accessed January 24, 2024], 9 August 2012. [Online]. Available: https://commons.wikimedia.org/wiki/File:Substitutional_solute.svg.

[18] Siamrut, *Interstitial solute*, https://upload.wikimedia.org/wikipedia/commons/1/19/Interstitial_solute.svg, [accessed January 24, 2024], 2012. [Online]. Available: https://commons.wikimedia.org/wiki/File:Interstitial_solute.svg.

[19] W. D. Callister and D. G. Rethwisch, *'STRENGTHENING BY GRAIN SIZE REDUCTION ,' in Materials science and engineering*, 9th ed. USA: Wiley, 2013, ch. 7, p. 229.

[20] Corrosionpedia. "Work hardening." corrosionpedia. Accessed: February 4, 2024. (2020), [Online]. Available: https://www.corrosionpedia.com/definition/1183/work-hardening.

[21] W. D. Callister and D. G. Rethwisch, *'INTERFACIAL DEFECTS ,' in Materials science and engineering*, 9th ed. USA: Wiley, 2013, ch. 7, p. 234.

[22] Cdang, *Courbe traction ecrouissage*, https://upload.wikimedia.org/wikipedia/commons/5/54/Courbe_traction_ecrouissage.svg, [accessed February 13, 2024], 13 January 2016. [Online]. Available: https://commons.wikimedia.org/wiki/File:Courbe_traction_ecrouissage.svg.

[23] W. D. Callister and D. G. Rethwisch, *' PRECIPITATION HARDENING,' in Materials science and engineering*, 9th ed. USA: Wiley, 2013, ch. 11, p. 451.

[24] J. R. Davis, *'Heat treating,' in Aluminum and Aluminum alloys*, 1st ed. USA: ASM International, 1994, ch. 3, p. 292.

[25] Cdang, *Diag eutectique cristallo refroidissement dans zone influence*, https://upload.wikimedia.org/wikipedia/commons/f/f8/Diag_eutectique_cristallo_refroidissement_dans_zone_influence.svg, [accessed February 13, 2024], 4 June 2009. [Online]. Available: https://commons.wikimedia.org/wiki/File:Diag_eutectique_cristallo_refroidissement_dans_zone_influence.svg.

[26] W. D. Callister and D. G. Rethwisch, *'Mechanism of hardening,' in Materials science and engineering*, 9th ed. USA: Wiley, 2013, ch. 11, pp. 455–457.

[27] A. Onat, "Effects of artificial aging heat treatment on mechanical properties and corrosion behaviour of aa6xxx aluminium alloys," *Journal of Chemical Engineering and Materials Science*, vol. 9, p. 18, Sep. 2018. DOI: 10.5897/JCEMS2018.0315.

[28] H. Farh, T. Ziar, H. Belghit, M. Khechba, A. E. Noua, and F. Serradj, "The cold rolling effect on the precipitation sequence and microstructural changes of an al-mg-si alloy," *Defect and Diffusion Forum*, vol. 397, pp. 51–58, Sep. 2019. DOI: 10.4028/www.scientific.net/DDF.397.51. [Online]. Available: https://www.researchgate.net/publication/336004451_The_Cold_Rolling_Effect_on_the_Precipitation_Sequence_and_Microstructural_Changes_of_an_Al-Mg-Si_Alloy.

[29] S. P. Ringer, B. C. Muddle, and I. J. Polmear, "Effects of cold work on precipitation in al-cu-mg-(ag) and al-cu-li-(mg-ag) alloys," *Metallurgical and Materials Transactions A*, vol. 26, no. 7, pp. 1659–1671, Jul. 1995, ISSN: 1543-1940. DOI: https://doi.org/10.1007/BF02670753.

[Online]. Available: https://link.springer.com/article/10.1007/BF02670753.

[30] A. Deschamps and Y. Brechet, "Influence of predeformation and ageing of an al–zn–mg alloy—ii. modeling of precipitation kinetics and yield stress," *Acta Materialia*, vol. 47, no. 1, 1998, ISSN: 1359-6454. DOI: https://doi.org/10.1016/S1359-6454(98)00296-1. [Online]. Available: https://www.sciencedirect.com/science/article/pii/S1359645498002961.

[31] D. Irmer, C. Moussa, L. T. Belkacemi, M. Sennour, A. Vaissière, and V. A. Esin, "Effect of cold rolling on nucleation, growth and coarsening of s-phase precipitates in al- cu- mg alloy (aa2024): From heterogeneous nucleation to homogeneous spatial distribution," *Journal of Alloys and Compounds*, vol. 963, 2023, ISSN: 0925-8388. DOI: https://doi.org/10.1016/j.jallcom.2023.171162. [Online]. Available: https://www.sciencedirect.com/science/article/pii/S0925838823024659.

[32] W. D. Callister and D. G. Rethwisch, *'ANISOTROPY,' in Materials science and engineering*, 9th ed. USA: Wiley, 2013, ch. 3, p. 86.

[33] A. Kumar, *Cold rolling*, https://upload.wikimedia.org/wikipedia/commons/c/cd/COLD-ROLLING.jpg, [accessed February 25, 2024], 11 February 2020. [Online]. Available: https://commons.wikimedia.org/wiki/File:COLD-ROLLING.jpg.

[34] TWI, *What is tensile testing?* Accessed: February 25, 2024. [Online]. Available: https://www.twi-global.com/technical-knowledge/faqs/what-is-tensile-testing.

[35] Nicoguaro, *Stress strain ductile*, https://upload.wikimedia.org/wikipedia/commons/c/c1/Stress_strain_ductile.svg, [accessed February 26, 2024], 5 May 2020. [Online]. Available: https://commons.wikimedia.org/wiki/File:Stress_strain_ductile.svg.

[36] W. D. Callister and D. G. Rethwisch, *'Tensile properties, Ductility,' in Materials science and engineering*, 9th ed. USA: Wiley, 2013, ch. 6, p. 184.

[37] W. D. Callister and D. G. Rethwisch, *'Tensile properties, Tougness,' in Materials science and engineering*, 9th ed. USA: Wiley, 2013, ch. 6, pp. 186–187.

[38] W. D. Callister and D. G. Rethwisch, *'Hardness,' in Materials science and engineering*, 9th ed. USA: Wiley, 2013, ch. 6, p. 191.

[39] *Metalliske materialer : Vickers-hardhetsmåling = metallic materials : Vickers hardness test : Part 1 : Test method (iso 6507-1:2018) : Del 1 : Prøvingsmetode (iso 6507-1:2018)*, eng, Lysaker: Standard Norge, 2016.

[40] Katsiv, *Vickerhard*, https://upload.wikimedia.org/wikipedia/commons/6/6f/Vickerhard.JPG, [accessed February 29, 2024], 3 December 2006. [Online]. Available: https://commons.wikimedia.org/wiki/File:Vickerhard.JPG.

[41] 'Struers', *About grinding and polsishing*, [accessed March 2, 2024]. [Online]. Available: https://www.struers.com/en/Knowledge/Grinding-and-polishing.

[42] 'Struers', *About etching*, [accessed March 2, 2024]. [Online]. Available: https://www.struers.com/en/Knowledge/Etching.

[43] Brandon, "What is scanning electron microscopy? (how it works, applications, and limitations)," Accessed: March 6, 2024. [Online]. Available: https://msestudent.com/what-is-scanning-electron-microscopy-how-it-works-applications-and-limitations/.

[44] Dake, *Sem electrons photons*, https://upload.wikimedia.org/wikipedia/commons/e/e1/Sem_electrons_photons.svg, [accessed March 2, 2024], 11 February 2006. [Online]. Available: https://commons.wikimedia.org/wiki/File:Sem_electrons_photons.svg.

[45] O. I. Group. "What is eds/edx analysis?" Accessed: March 2, 2024. (), [Online]. Available: https://nano.oxinst.com/campaigns/what-is-eds/edx.

[46] FDominec, *Edx of a poppy seed*, https://upload.wikimedia.org/wikipedia/commons/7/77/EDX_of_a_poppy_seed.jpg, [accessed March 2, 2024], 16 September 2019. [Online]. Available: https://commons.wikimedia.org/wiki/File:EDX_of_a_poppy_seed.jpg.

[47] B. Inkson. "Electron backscatter diffraction." [Section: 2.7.3 Surface crystallography; Accessed: March 8, 2024]. (2016), [Online]. Available: https://www.sciencedirect.com/topics/materials-science/electron-backscatter-diffraction.

[48] Brandon, "What is scanning electron microscopy? (how it works, applications, and limitations)," [Section: EBSD (Electron Backscatter Diffraction); Accessed: March 2, 2024]. [Online]. Available: https://msestudent.com/what-is-scanning-electron-microscopy-how-it-works-applications-and-limitations/.

[49] BenBritton, *Ebsd si*, https://upload.wikimedia.org/wikipedia/commons/4/44/EBSD_Si.png, [accessed March 7, 2024]. [Online]. Available: https://commons.wikimedia.org/wiki/File:EBSD_Si.png.

[50] *Standard test methods for tension testing of metallic materials: Fig. 1 rectangular tension test specimens*, eng, An American National Standard, 2004.

[51] *Metalliske materialer : Strekkprøving = metallic materials : Tensile testing : Part 1 : Method of test at room temperature (iso 6892-1:2016) : Del 1 : Metode for prøving ved romtemperatur (iso 6892-1:2016)*, eng, Lysaker: Standard Norge, 2016.

[52] W. D. Callister and D. G. Rethwisch, *'Grain-Size Determination', in Materials science and engineering*, 9th ed. USA: Wiley, 2013, ch. 11, p. 128.

A Appendix A - Hardness test

A.1 Original plate

The table below presents the hardness values of sample IS in planes ACR and PCR.

Table A.1: Hardness values (HV10) for sample IS in ACR and PCR planes.

Samples	Indent.1	Indent.2	Indent.3	Indent.4	Indent.5
IS-ACR	54.11	54.44	54.68	55.54	55.36
IS-PCR	52.66	53.62	55.23	53.90	54.20

A.2 Artificial ageing

The tables below present hardness values of samples 0-AA, 30-AA and 60-AA after artificial ageing in planes ACR and PCR.

Table A.2: Hardness values (HV10) for sample 0-AA in ACR and PCR planes.

Samples	Indent.1	Indent.2	Indent.3	Indent.4	Indent.5
0-AA-ACR	100.5	100.5	104.1	101.7	103.1
0-AA-PCR	97.18	96.71	101.7	104.0	98.7

Table A.3: Hardness values (HV10) for sample 30-AA in ACR and PCR planes.

Samples	Indent.1	Indent.2	Indent.3	Indent.4	Indent.5
30-AA-ACR	120.4	120.9	122.9	121.8	124.8
30-AA-PCR	129.60	125.90	127.80	125.10	128.10

Table A.4: Hardness values (HV10) for sample 60-AA in ACR and PCR planes.

Samples	Indent.1	Indent.2	Indent.3	Indent.4	Indent.5
60-AA-ACR	125.3	125.80	126.0	126.9	126.2
60-AA-PCR	131.50	133.80	134.90	131.90	131.80

A.3 Natural ageing

The tables below present the hardness values of samples 0-NA, 30-NA, and 60-NA in plane PCR at room temperature over different time intervals.

Table A.5: Hardness values (HV10) of sample 0-NA in plane PCR over different time intervals.

Time	Indent.1	Indent.2	Indent.3	Indent.4	Indent.5
after 1-hour	67.28	66.72	67.64	66.19	66.34
after 3-hour	70.34	72.33	73.75	72.53	71.97
after 7.5-hour	78.31	76.58	78.61	79.10	78.57
after 1-day	80.38	81.52	79.87	80.34	81.28
after 2-day	81.68	82.16	86.65	84.85	82.53
after 1-week	89.34	88.56	90.16	86.35	87.22
after 2-week	88.97	88.16	90.68	88.25	89.93

Table A.6: Hardness values (HV10) of sample 30-NA in plane PCR over different time intervals.

Time	Indent.1	Indent.2	Indent.3	Indent.4	Indent.5
after 1-hour	92.87	91.52	91.48	89.24	91.67
after 3-hour	94.84	92.87	92.29	92.77	93.26
after 7.5-hour	95.69	97.39	98.65	94.29	96.10
after 1-day	100.90	101.30	103.40	99.24	102.50
after 2-day	102.80	103.10	99.24	101.20	103.90
after 1-week	106.00	105.60	103.80	103.90	106.90
after 2-week	104.20	106.00	106.20	103.10	107.40

Table A.7: Hardness values (HV10) of sample 60-NA in plane PCR over different time intervals.

Time	Indent.1	Indent.2	Indent.3	Indent.4	Indent.5
after 1-hour	104.00	102.50	103.00	103.90	105.60
after 3-hour	106.10	107.20	108.00	109.70	108.90
after 7.5-hour	109.40	112.30	110.40	110.50	110.20
after 1-day	111.20	112.90	117.40	113.50	116.6
after 2-day	114.60	115.60	114.50	117.40	115.10
after 1-week	119.20	116.70	116.00	116.70	118.70
after 2-week	116.50	116.50	117.30	118.50	119.00

B Appendix B - Tensile test graphs

B.1 Sample IS

B.1.1 Samples IS in ACR direction

Table B.1: Yield, tensile strength and strain for samples in ACR direction.

Samples	$(R_p0.2)$(MPa)	R_m(MPa)	Strain(%)
A-IS-1	140	146	11.7
A-IS-2	139	145	12.41
A-IS-3	139	145	12.57

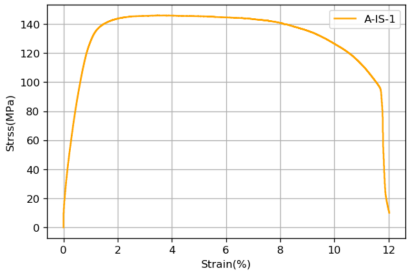

(a) A-IS-1

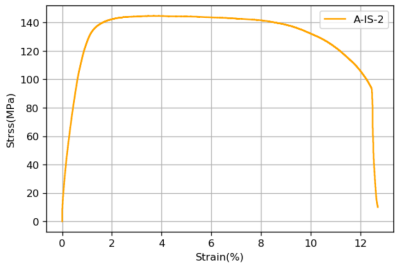

(b) A-IS-2

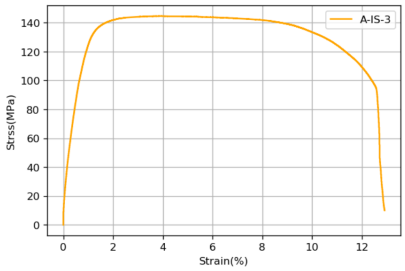

(c) A-IS-3

Figure B.1: Stress-strain diagrams for three samples in ACR direction.

B.1.2 Samples IS in PCR direction

Table B.2: Yield, tensile strength and strain for samples in PCR direction.

Samples	$(R_p0.2)$(MPa)	R_m(MPa)	Strain(%)
P-IS-1	144	149	8.67
P-IS-2	144	149	8.457
P-IS-3	144	149	8.73

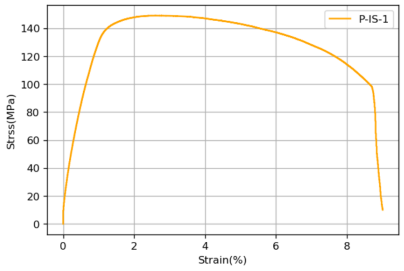

(a) P-IS-1

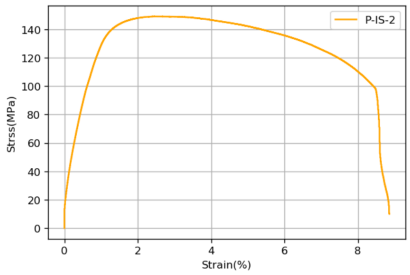

(b) P-IS-2

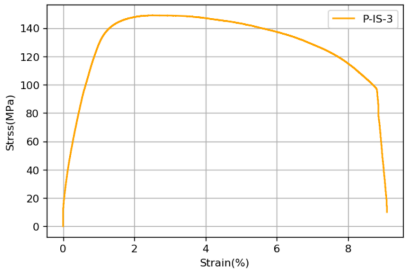

(c) P-IS-3

Figure B.2: Stress-strain diagrams for three samples in PCR direction.

B.2 Sample 0 %

B.2.1 Samples 0 % in ACR direction

Table B.3: Yield, tensile strength and strain for samples in ACR direction.

Samples	$(R_p0.2)$(MPa)	R_m(MPa)	Strain(%)
A-0-1	173	272	22.75
A-0-2	175	274	23.09
A-0-3	175	274	21.65

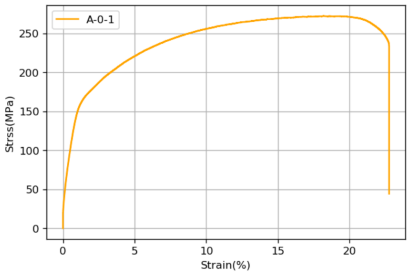

(a) A-0-1

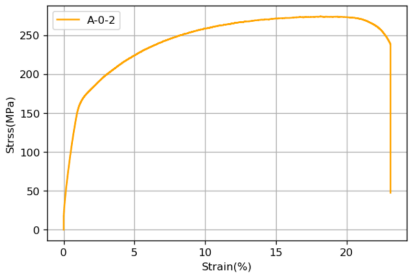

(b) A-0-2

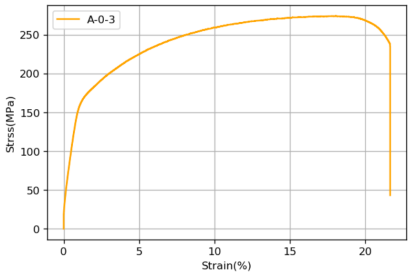

(c) A-0-3

Figure B.3: Stress-strain diagrams for three samples in ACR direction.

B.2.2 Samples 0 % in PCR direction

Table B.4: Yield, tensile strength and strain for samples in PCR direction.

Samples	$(R_p0.2)$(MPa)	R_m(MPa)	Strain(%)
P-0-1	174	273	23.12
P-0-2	179	274	21.21
P-0-3	174	273	21.08

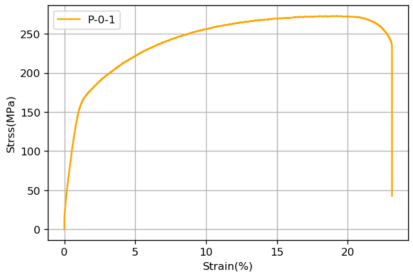

(a) P-0-1

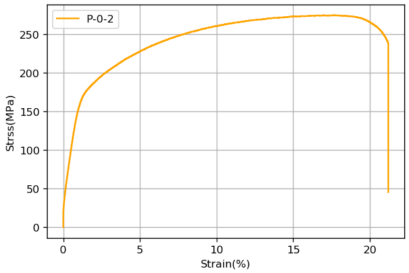

(b) P-0-2

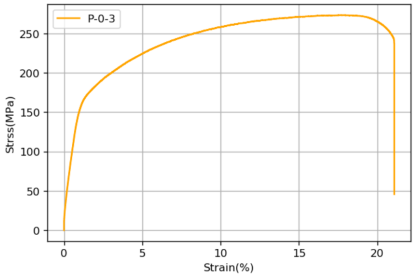

(c) P-0-3

Figure B.4: Stress-strain diagrams for three samples in PCR direction.

B.3 Sample 30 %

B.3.1 Samples 30 % in ACR direction

Table B.5: Yield, tensile strength and strain for samples in ACR direction.

Samples	$(R_p0.2)$(MPa)	R_m(MPa)	Strain(%)
A-30-1	324	339	11.33
A-30-2	321	340	11.62
A-30-3	319	339	11.85

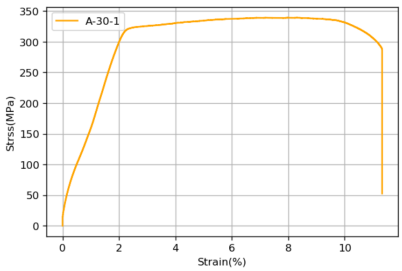

(a) A-30-1

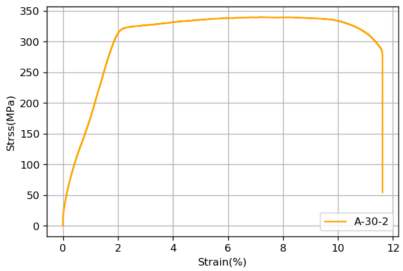

(b) A-30-2

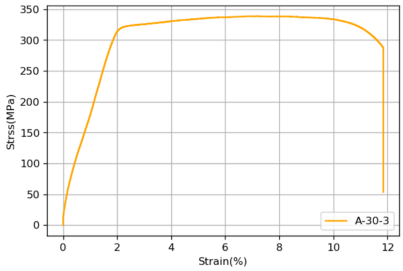

(c) A-30-3

Figure B.5: Stress-strain diagrams for three samples in ACR direction.

B.3.2 Samples 30 % in PCR direction

Table B.6: Yield, tensile strength and strain for samples in PCR direction.

Samples	$(R_p0.2)$(MPa)	R_m(MPa)	Strain(%)
P-30-1	305	329	9.66
P-30-2	306	330	9.96
P-30-3	307	331	10.13

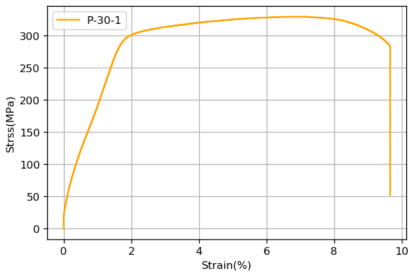

(a) P-30-1

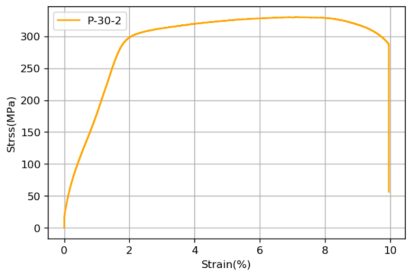

(b) P-30-2

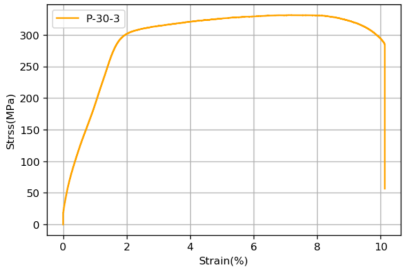

(c) P-30-3

Figure B.6: Stress-strain diagrams for three samples in PCR direction.

B.4 Sample 60 %

B.4.1 Samples 60 % in ACR direction

Table B.7: Yield, tensile strength and strain for samples in ACR direction.

Samples	$(R_p0.2)$(MPa)	R_m(MPa)	Strain(%)
A-60-1	342	367	10.99
A-60-2	338	362	11.92
A-60-3	341	366	10.49

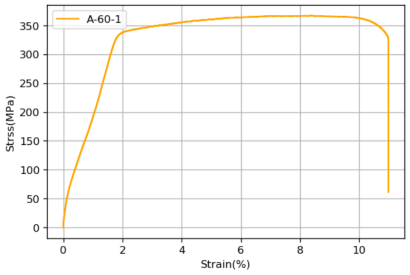

(a) A-60-1

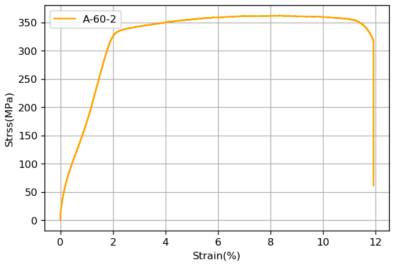

(b) A-60-2

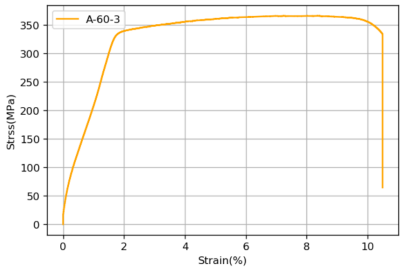

(c) A-60-3

Figure B.7: Stress-strain diagrams for three samples in ACR direction.

B.4.2 Samples 60 % in PCR direction

Table B.8: Yield, tensile strength and strain for samples in PCR direction.

Samples	$(R_p0.2)$(MPa)	R_m(MPa)	Strain(%)
P-60-1	324	345	7.51
P-60-2	325	346	7.44
P-60-3	329	348	6.9

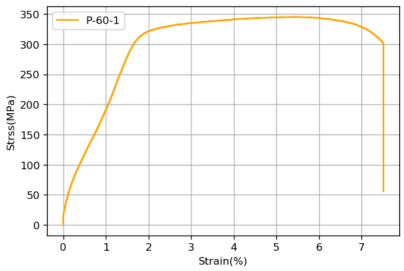

(a) P-60-1

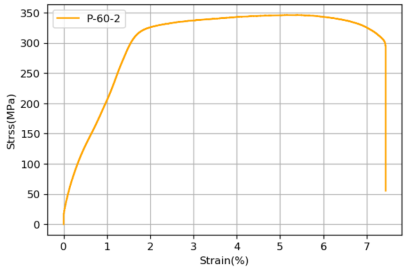

(b) P-60-2

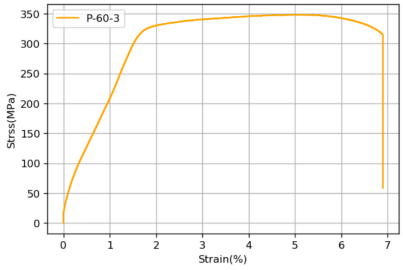

(c) P-60-3

Figure B.8: Stress-strain diagrams for three samples in PCR direction.

C Appendix C - Grain size

C.1 Sample 0 %

Chart: Grain Size (Intercept Lengths)

Edge grains included in analysis as half grains
2538 grain intercepts sampled
119 Lines
Average Intercept length = 55.539 microns

Intercept Length [microns]	Number Fraction
16.55	0.540189
45.65	0.161939
74.75	0.0886525
103.85	0.070134
132.95	0.0319149
162.05	0.037037
191.15	0.0181245
220.25	0.0161545
249.35	0.00906225
278.45	0.00945626
307.55	0.00236407
336.65	0.00433412
365.75	0.00275808
394.85	0.00315209
423.95	0.00275808
453.05	0.000394011
482.15	0.000788022
511.25	0
540.35	0.000394011
569.45	0.000394011
Average Number	55.539
Standard Deviation Number	73.4487

(a) Numerical data

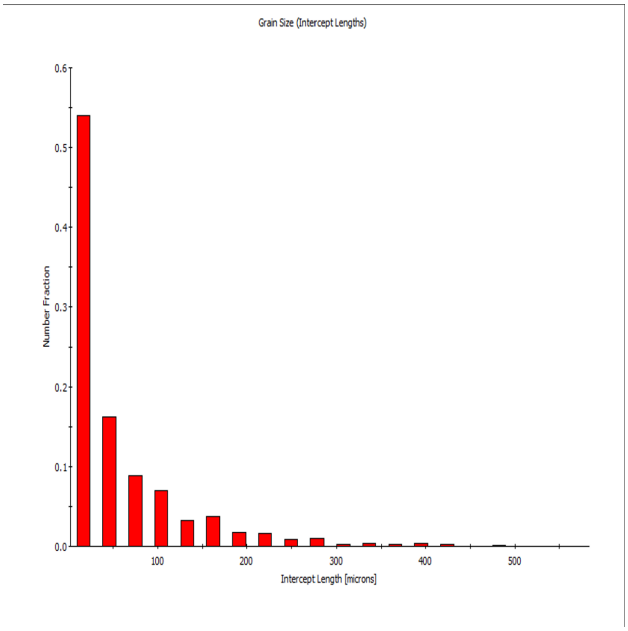

(b) Bar plot

Figure C.1: Result of grain size determination for sample 0 %

C.2 Sample 30 %

Chart: Grain Size (Intercept Lengths)

Edge grains included in analysis as half grains
3628 grain intercepts sampled
119 Lines
Average Intercept length = 39.691 microns

Intercept Length [microns]	Number Fraction
25.15	0.76957
71.45	0.101985
117.75	0.0540243
164.05	0.030871
210.35	0.0157111
256.65	0.0115766
302.95	0.00799339
349.25	0.00441014
395.55	0.00110254
441.85	0.00110254
488.15	0.000551268
534.45	0.000551268
580.75	0
627.05	0
673.35	0
719.65	0
765.95	0.000275634
812.25	0
858.55	0
904.85	0.000275634
Average Number	39.6913
Standard Deviation Number	66.6317

(a) Numerical data

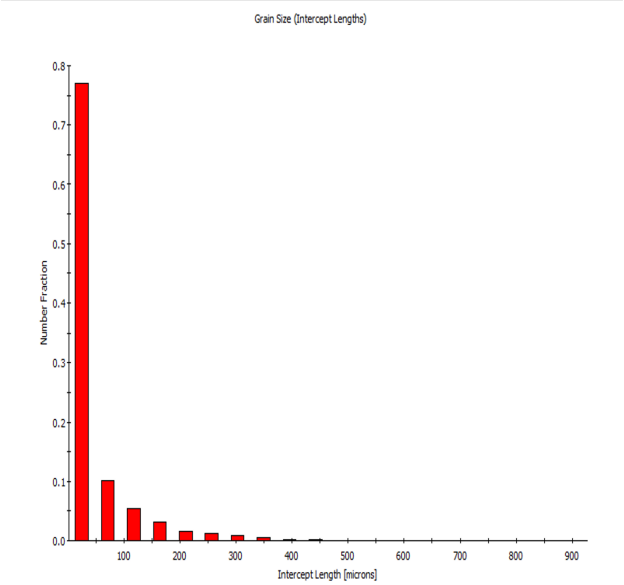

(b) Bar plot

Figure C.2: Result of grain size determination for sample 30 %

C.3 Sample 60 %

Chart: Grain Size (Intercept Lengths)

Edge grains included in analysis as half grains
8179 grain intercepts sampled
119 Lines
Average Intercept length = 17.577 microns

Intercept Length [microns]	Number Fraction
14.5	0.847414
39.5	0.0737254
64.5	0.0279985
89.5	0.0165057
114.5	0.0101479
139.5	0.00794718
164.5	0.00489057
189.5	0.00293434
214.5	0.00207849
239.5	0.00134491
264.5	0.000978115
289.5	0.00110038
314.5	0.000611322
339.5	0.000611322
364.5	0.00085585
389.5	0.000122264
414.5	0.000122264
439.5	0.000489057
464.5	0
489.5	0.000122264
Average Number	17.5767
Standard Deviation Number	36.6679

(a) Numerical data

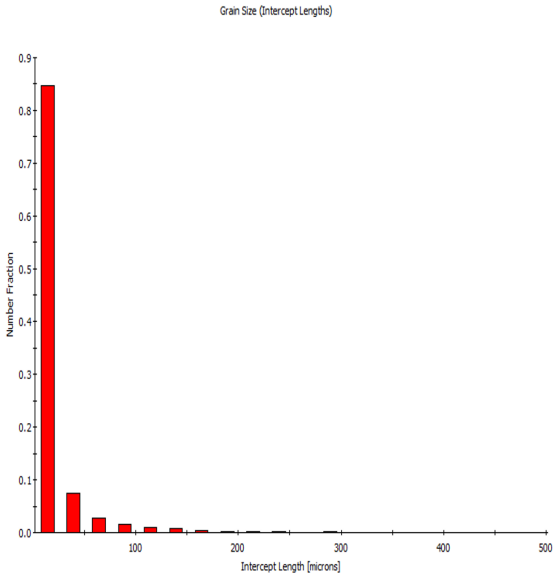

(b) Bar plot

Figure C.3: Result of grain size determination for sample 60 %